
Article:
Burkle, D, De Motte, R, Taleb, W orcid.org/0000-0003-2179-7963 et al. (5 more authors) (2017) In situ SR-XRD study of $FeCO_3$ precipitation kinetics onto carbon steel in CO_2-containing environments: The influence of brine pH. Electrochimica Acta, 255. pp. 127-144. ISSN 0013-4686

https://doi.org/10.1016/j.electacta.2017.09.138

Title: *In situ* SR-XRD study of $FeCO_3$ precipitation kinetics onto carbon steel in CO_2-containing environments: The influence of brine Ph

Authors: D. Burkle, R. De Motte, W. Taleb, A. Kleppe, T. Comyn, S.M. Vargas, A. Neville, R. Barker

PII: S0013-4686(17)32009-1
DOI: https://doi.org/10.1016/j.electacta.2017.09.138
Reference: EA 30337

To appear in: *Electrochimica Acta*

Received date: 14-4-2017
Revised date: 21-9-2017
Accepted date: 22-9-2017

Please cite this article as: D.Burkle, R.De Motte, W.Taleb, A.Kleppe, T.Comyn, S.M.Vargas, A.Neville, R.Barker, In situ SR-XRD study of FeCO3 precipitation kinetics onto carbon steel in CO2-containing environments: The influence of brine Ph, Electrochimica Acta https://doi.org/10.1016/j.electacta.2017.09.138

In situ SR-XRD study of $FeCO_3$ precipitation kinetics onto carbon steel in CO_2-containing environments: The influence of brine pH

D. Burkle,[a*] R. De Motte,[a] W. Taleb,[a] A. Kleppe,[b] T. Comyn,[c] S. M. Vargas,[d] A. Neville,[a] and R. Barker[a]

[a]Institute of Functional Surfaces, School of Mechanical Engineering, University of Leeds, Leeds, LS2 9JT, United Kingdom.
[b]Diamond Light Source Ltd, Diamond House, Didcot, Oxfordshire, OX11 ODE United Kingdom.
[c]Ionix Advanced Technologies, 3M Buckley Innovation Centre, Firth Street, Huddersfield, HD1 3BD, United Kingdom.
[d]BP America, Inc., Houston, Texas 77079, United States of America.

[*]**Corresponding Author**

ABSTRACT

The growth of iron carbonate ($FeCO_3$) on the internal walls of carbon steel pipelines used for oil and gas transportation can reduce internal corrosion significantly. Solution pH can be considered as one of the most influential factors with regards to the kinetics, morphology and protection afforded by $FeCO_3$ films. This paper presents results from a recently developed in situ Synchrotron Radiation-X-ray Diffraction (SR-XRD) flow cell integrated with electrochemistry for corrosion measurements. The cell was used to follow the nucleation and growth kinetics of corrosion products on X65 carbon steel surfaces in a carbon dioxide (CO_2)-saturated 3.5 wt.% NaCl brine at 80°C and a flow rate of 0.1 m/s over a range of solution pH values (6.3, 6.8 and 7). In all conditions, $FeCO_3$ was identified as the only crystalline phase to form. Electrochemical results coupled with post-test surface analysis indicate that at higher pH, larger portions of the surface become covered faster with thinner, more protective films consisting of smaller, denser and more compact crystals. The comparison between XRD main peak area intensities and $FeCO_3$ surface coverage, mass and volume indicates a qualitative relationship between these parameters at each pH, providing valuable information on the kinetics of film growth.

Key words: CO_2 corrosion, pH, iron carbonate, precipitation, synchrotron, X-ray diffraction

1. INTRODUCTION

The presence of dissolved carbon dioxide (CO_2) in oilfield production fluids is known to promote the internal general and localised corrosion of carbon steel pipelines through the formation of carbonic acid (H_2CO_3). In particular, the potential for severe localised attack of carbon steel in CO_2-containing conditions inevitably leads to concerns over pipeline integrity during service when transporting hydrocarbons. Observations of localised degradation are particularly evident under conditions where protective iron carbonate ($FeCO_3$) films have only partially formed on or been removed from a steel surface, as this has been shown to lead to the development of galvanic cells between the filmed area (cathode) and bare steel (anode) [1-3]. Understanding the fundamental processes governing the formation of $FeCO_3$ and conditions conducive to it local mechanical and/or chemical removal is essential in developing a robust and reliable corrosion management strategy for transportation pipelines. The formation of $FeCO_3$ on the internal walls of carbon steel pipelines in CO_2 environments is not an uncommon observation in the oil and gas industry. When the concentration of iron ions (Fe^{2+}) and carbonate ions (CO_3^{2-}) exceed the solubility product (K_{sp}) of $FeCO_3$ in a solution, it becomes thermodynamically possible for $FeCO_3$ to precipitate onto the internal walls of pipelines [4]:

$$Fe^{2+}_{(aq)} + CO^{2-}_{3\,(aq)} \rightarrow FeCO_{3\,(s)} \quad (1)$$

The $FeCO_3$ precipitation process can dramatically reduce the corrosion kinetics of the underlying steel by offering a diffusion barrier to electrochemically active species and by blocking active sites on the steel surface [5]. However, the nature, morphology and protection offered by such films are dependent upon both environmental and operating conditions. In

particular, factors which influence the precipitation rate of $FeCO_3$ can have a profound effect on how effectively the film is able to suppress corrosion kinetics of the underlying steel.

$FeCO_3$ nucleation and growth is governed by the saturation ratio, S_{FeCO_3}, which is deemed to be the driving force behind the precipitation process [6]. S_{FeCO_3} is defined as:

$$S_{FeCO_3} = \frac{[Fe^{2+}][CO_3^{2-}]}{K_{sp}} \quad (2)$$

where $[Fe^{2+}]$ and $[CO_3^{2-}]$ (in mol/m^3) are the concentrations of ferrous and carbonate ions, respectively. K_{sp} (in mol^2/m^6) is the solubility product for $FeCO_3$, which is a function of ionic strength and temperature. At higher solution pH, higher concentrations of CO_3^{2-} result in fewer Fe^{2+} ions being required to exceed the solubility product of $FeCO_3$, and generate significant levels of precipitation [7].

The nucleation and growth of the $FeCO_3$ layer is heavily dependent upon the kinetics of the precipitation reaction which are governed by the surrounding environment. Such a process is facilitated when $S_{FeCO_3} > 1$ [8]. Although nuclei formation is thermodynamically possible at $S_{FeCO_3} > 1$, its rate increases rapidly only when a critical S_{FeCO_3} is exceeded [9]. The process of nucleation starts with heterogeneous nucleation, a process which is capable of occurring easily due to the numerous imperfections on the steel surface [10]. Nucleation is then followed by crystal growth which essentially limits the rate of precipitation.

As previously stated, the protectiveness of $FeCO_3$ is influenced by several environmental factors such as temperature, pH, CO_2 partial pressure and Fe^{2+} concentration. From all the parameters, solution pH can be regarded as one of the most important factors. As an example, Chokshi et al.[11] demonstrated that for the corrosion of carbon steel in a pH 6 at 80°C in a CO_2-saturated 1 wt.% NaCl brine with an addition of 50 ppm Fe^{2+}, a low bulk S_{FeCO_3} was obtained resulting in the formation of a porous, detached and poorly protecting $FeCO_3$ film forming on

the steel surface resulting in a final corrosion rate of 1.8 mm/yr after 45 hours. Higher pH values of 6.6 under the same operating conditions (80°C, 1wt. % NaCl, 50 ppm Fe^{2+}) resulted in a higher bulk S_{FeCO_3}, faster precipitation kinetics and formation of a more protective $FeCO_3$ film resulting in a final corrosion rate of 0.1 mm/yr after 45 hours.

As well as influencing the precipitation kinetics of $FeCO_3$, pH can also have a profound effect on the size and morphology of the crystals by influencing S_{FeCO_3} and hence, crystal nucleation and growth, which in turn influences the level of protection offered by the $FeCO_3$ film. Pessu et al.[12] exposed X65 steel samples to a 3.5 wt.% NaCl solution at 50°C for 168 hours at three different pH levels of 3.8, 6.6 and 7.5. At pH 3.8 a porous, amorphous/nano-polycrystalline $FeCO_3$ film developed that offered minimal protection to the steel surface. Increasing pH to 6.6 resulted in a protective $FeCO_3$ film consisting of cubic crystals which grew progressively on the steel surface. The crystals were observed to be loosely packed on the steel surface. At pH 7.5, film formation was rapid and produced rhombohedral $FeCO_3$ crystals with sharp, well defined edges which were extremely protective and compact. As pH was increased, there was a notable increase in the density and compactness of the corrosion product layer, which linked strongly to the level of protection offered to the steel substrate. Similarly, Tanupabrungsun et al.[13] and Li et al.[14] demonstrate that protective $FeCO_3$ formation is accelerated/enhanced at higher solution pH, corroborating with the observations of Pessu et al.[12].

Understanding the formation, chemistry and role of CO_2-induced corrosion products in oilfield environments remains of considerable interest to industry. Providing clear links between the nature/protectiveness of films and defined operating conditions can provide reassurance over the adopted corrosion management strategies and improve the capabilities of corrosion prediction tools. Considering that pH plays a critical role in influencing both the kinetics of corrosion reactions as well as the morphology and composition of corrosion products, the present paper focuses on examining the influence of solution acidity/alkalinity on the early

stages of film development. However, one key challenge in studying $FeCO_3$ precipitation is following the growth kinetics and relating this to the corrosion rate of the steel substrate either in a quantitative or qualitative manner. Therefore, in this work, we demonstrate the capabilities of in situ Synchrotron Radiation-X-Ray Diffraction (SR-XRD) to study the film growth processes with a custom designed flow cell which is described in our previous publication [15]. The flow cell has been designed to enable simultaneous acquisition of diffraction patterns and electrochemical corrosion measurements from the steel surface. This enables the kinetics of film formation to be followed and correlated with the corrosion rate of the steel substrate in real-time in a flowing system.

A number of research groups have already studied the formation of corrosion products in CO_2 corrosive environments using in situ SR-XRD [16-20]. Such studies have reported that in simple CO_2-containing brine solutions a number of iron oxides/hydroxide phases form in conjunction with $FeCO_3$. Such phases include magnetite (Fe_3O_4) [21], chukanovite ($Fe_2(OH)_2CO_3$) [16-20], wustite (FeO) [20] and goethite (FeO(OH)) [20]. However, these studies have either been performed in oxygen contaminated systems (as suggested by the authors themselves) [20], or the growth of the corrosion product was accelerated by applying excessive currents/voltages (unlike in this research) to the sample under study [18, 19] which were not realistic of the actual corrosion kinetics encountered in the field and consequently prevented the true processes of film formation from being established. Additionally, none of the aforementioned studies have examined corrosion product growth in a flowing system.

In the present research, the flow cell is used to assess the effect that pH has on the early kinetics of $FeCO_3$ film formation and demonstrates that at the very least, qualitative information can be obtained on the rate of film growth which can also be related to the corrosion rate transient response of the carbon steel substrate. Further laboratory studies are also presented to supplement the observations in the Synchrotron facility. These include ex situ Scanning

Electron Microscopy (SEM) analysis which was performed on samples at different time intervals of the experiments, as well as longer term electrochemical corrosion measurements. From the SEM images acquired, the surface coverage and size of the crystals were evaluated in order to gain information relating to the induction time, as well as the nucleation and growth processes identified through the in situ X-ray and electrochemical measurements.

2. EXPERIMENTAL

The following sections provide information relating to the experimental approach and the test conditions evaluated using the SR-XRD flow cell. The flow cell design is described in detail in our previous publication [15], which also discusses the setup, operation and full capabilities of the system. However, a brief summary of the setup and operation is provided here for completeness.

2.1 SR-XRD flow cell experimental set-up

A schematic diagram of the flow cell setup at the Diamond Light Source, Oxfordshire, UK as well as an image taken in the experimental hutch itself is shown in Figure 1. A locally heated formation brine circulates within a closed loop between the flow cell and a 1L vessel via the use of a centrifugal micro-pump. The flow cell houses a carbon steel sample (or working electrode) from which diffraction patterns and electrochemical responses are recorded. A detailed description of the components within the system (including the platinum counter and Ag/AgCl reference electrode configuration) is provided in the paper by Burkle et al.[15]. Suffice to say that the main capabilities of the system are that it enables in situ electrochemical measurement and SR-XRD measurements to be collected continuously from the carbon steel sample within the cell throughout the duration of the test without disturbing the flow conditions i.e. diffraction patterns can be acquired through the flowing brine.

Once flow was initiated through the cell, electrochemical and SR-XRD measurements commenced after 3-4 minutes from when the pump was switched on as this was the time taken to complete the safety checks and evacuate the experimental hutch. Each of the experiments conducted at the Synchrotron facility ran for a duration of 4 hours. Additional tests using the cell ran for 20 hours and were conducted in University of Leeds corrosion laboratories.

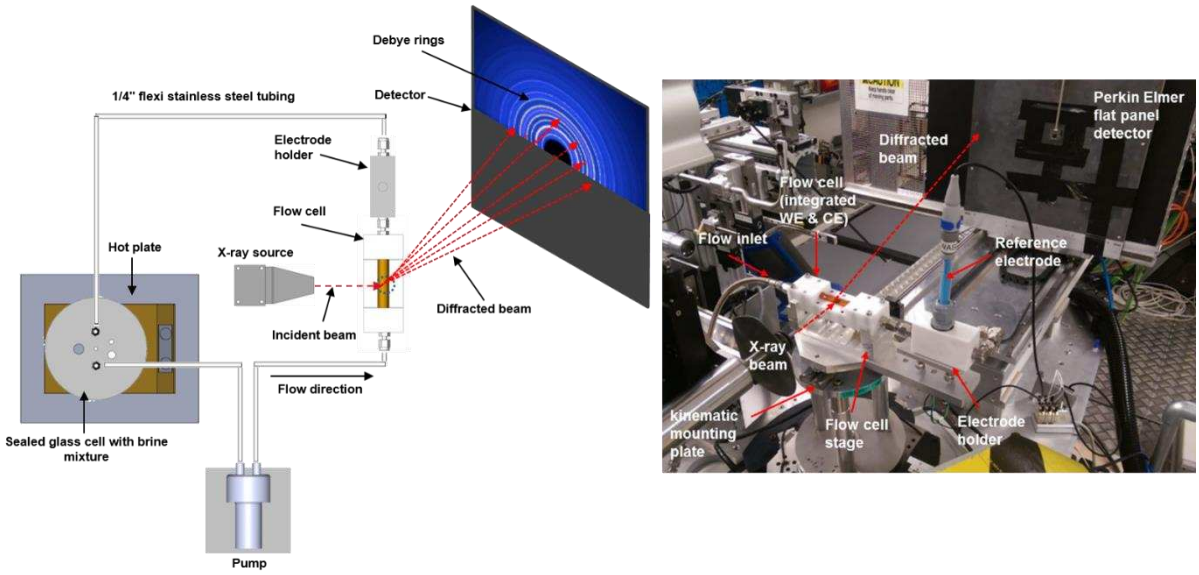

Figure 1. The flow cell set-up during Synchrotron experiments: Photograph (right) and schematic (left) of the flow cell set-up used on the Diamond Light Source beamline (I15).

2.2 Materials

The samples fitted into the flow cell throughout this study were made from X65 grade carbon steel. The steel was provided in bar form and machined into cylinders of 9 mm diameter and 10 mm length. The exposed surface area of the sample to the 1L of electrolyte was 0.63 cm^2 for each experiment. The carbon steel samples used comprised of pearlite and ferrite phases with approximately 10-13% consisting of pearlite which was randomly dispersed within the face of the sample exposed to the test solution. The chemical composition of the steel was (in wt.%): C 0.15, Mn 1.422, Ni 0.09, Nb 0.054, Mo 0.17, Si 0.22, V 0.06, P 0.025, S 0.002, Fe balance. Prior to the start of the experiment, the test sample was wet-ground up to 600 silicon

carbide grit paper, degreased with acetone, rinsed with distilled water and dried with compressed air before being immediately flush mounted into the base of the flow cell. An electrical wire was then connected to the base of the sample to enable connection to a potentiostat for electrochemical measurements.

2.3 Brine preparation and operating conditions

For all experiments, the test solution used was a CO_2-saturated 3.5 wt.% NaCl solution. To achieve de-aeration and minimise the dissolved oxygen concentration (O_2), the test solution was purged with high purity CO_2 for a minimum of 4 hours prior to each experiment. In addition, high purity CO_2 was continuously bubbled into the test solution throughout the entire duration of each experiment. The flow cell and brine vessel were also sealed with one small outlet for CO_2 gas to prevent O_2 ingress. Based on colorimetric analysis of the test solution, the concentration of O_2 was determined to be below 50 pbb. Each test was conducted at a fixed temperature of 80 ± 1ºC and flow velocity of 0.1 m/s. The only parameter changed between each test was the solution pH which was varied for each experiment and controlled through the addition of sodium bicarbonate ($NaHCO_3$) with the aid of an automatic temperature correction pH probe. Three pH values of 6.3, 6.8 and 7.0 were assessed within this study.

2.3. Data acquisition: XRD and Electrochemistry

2.3.1. Collection and interpretation of XRD data

The in situ SR-XRD experiments were conducted at beamline I15 at the Diamond Light Source. Synchrotron radiation was adjusted and focused into a monochromatic beam (70 µm in diameter) with a well-defined energy of 40 keV and a corresponding wavelength (λ) of 0.3099 Å. The incident-beam to sample angle was set to 4º. In order to maximise the accuracy and the ability of the XRD patterns to be correlated with the extent of crystal growth, an operational loop was devised to scan five measurements over a 2 mm path length across the centre of each

sample for every experiment. The reason behind implementing such a technique is that the crystal formation may not be entirely uniform across the steel surface, particularly in the early stages of growth. Consequently, this method of analysis enables identification of the consistency of film growth in different locations across the steel, but also provides a larger sampling size from the surface which can be more accurately and reliably correlated with ex situ measurements (e.g. SEM images and corrosion product mass measurements as a function of time). In this work, both the transient response from individual scans, as well as the average from all 5 scanned areas are presented to describe the non-uniform growth characteristics over the surface and to provide the most representative data possible to correlate with the collected ex situ data.

With regards to the duration of data acquisition, individual data scans at each location took 60 seconds to acquire an XRD pattern (including the time taken for movement to each point). Therefore the overall scanning time to complete the 5 scans over a 2 mm path length was ~5 minutes. These diffraction images were recorded using a Perkin Elmer flat panel detector located 975 mm from the sample and conventional 2θ diffraction patterns were generated by radial integration of the Debye rings using the software Fit2D with subsequent data analysis performed by profile fitting and Rietveld analysis.

2.3.2 Collection and interpretation of electrochemical data

With regards to the electrochemical measurements, linear polarisation resistance (LPR) and electrochemical impedance spectroscopy (EIS) were employed to determine the in situ corrosion rate of the X65 carbon steel working electrode. LPR measurements were performed by polarising the sample ±15 mV vs. the open circuit potential (OCP) at a scan rate of 0.25 mV/s to obtain a polarisation resistance (R_p) and were undertaken every 5 minutes. In all of the experiments, the solution resistance (R_s) was measured independently in laboratory tests away from the Synchrotron beam using EIS. For these specific measurements, the sample was

polarised ±5 mV vs. the OCP using the frequency range from 20 kHz to 0.1 Hz. The value of R_s was subtracted from R_p to produce a charge-transfer resistance (R_{ct} in Ohm.cm^2) which was used to determine the corrosion rate behaviour with time.

$$R_{ct} = R_p - R_s \tag{3}$$

Potentiodynamic measurements were also performed within the flow cell on freshly ground samples in separate experiments at each solution pH. This technique was used to generate Tafel polarisation curves to determine the anodic and cathodic Tafel constants and ultimately an appropriate Stern-Geary coefficient (B) to enable calculation of corrosion rates from the values of R_{ct} determined as a function of time in each experiment. Tafel polarisation curves were collected by performing individual anodic and cathodic sweeps starting at OCP and scanning to +150 mV or -500 mV vs. OCP, respectively at a scan rate of 0.5 mV/s. Freshly wet-ground samples and new test solutions were used for each individual anodic and cathodic sweep. From the polarisation curves produced, it was possible to determine the anodic (β_a) and cathodic (β_c) Tafel constants in mV/decade by measuring their respective gradient over regions were linearity was observed between the applied voltage and the natural log of the measured current. The Tafel slope measurements were used in Equation (4) to determine the Stern-Geary coefficient (B), and the corrosion current density (i_{corr} in mA/cm^2) using Equation (5).

$$B = \frac{\beta_a \beta_c}{2.303(\beta_a + \beta_c)} \tag{4}$$

$$i_{corr} = \frac{B}{R_{ct}} \tag{5}$$

The i_{corr} value obtained through Equation (5) was then used in combination with Equation (6) (based on Faraday's Law) and the measured values of R_{ct} to determine the corrosion rate in mm/year:

$$CR = 3.27 \frac{i_{corr} M_{Fe}}{n\rho} \quad (6)$$

where 3.27 is a conversion factor (in (mm.g)/(mA.cm.year)), to obtain corrosion rate (CR) in units of mm/year, M_{Fe} is the molar mass of iron (55.8 g), n is the number of electrons freed in the corrosion reaction (2 electrons) and ρ is the density of steel (7.87 g/cm^3).

2.4. *Ex-situ* surface analysis

To supplement Synchrotron experiments, additional tests were performed away from the beamline in University of Leeds corrosion laboratories to enable ex situ data to be collected in the form of SEM images. These micrographs could then be correlated with the recorded XRD patterns and electrochemistry data obtained at the Synchrotron. The laboratory experiments varied in duration from 30 to 240 minutes depending upon the point at which samples were identified for removal. At the end of each experiment, the samples were rinsed with acetone, dried using compressed air and retained in a desiccator prior to SEM analysis, which was performed using a Hitachi TM3030 Bench Top SEM in secondary electron mode with an operating voltage of 15 kV. The SEM images were carefully analysed to determine the crystal morphology, crystal size and the surface coverage. The surface coverage was obtained through processing numerous random images from across the same surface into a MATLAB programme that utilises the difference in contrast of the crystals formed against the bare steel surface to produce a binary output image in black and white. Surface coverage was determined through recording the percentage of black pixels (crystals) against the white pixels (no crystals). This method of surface coverage analysis has been implemented and validated elsewhere through a previous publication [22]. In order to determine the corrosion product mass,

the mass of the samples after each experiment was recorded before and after removal of corrosion products from the steel surface using a sensitive micro balance (Mettler XP26). At the end of each experiment, the sample was removed from the flow cell and rinsed with acetone and then dried with compressed air. The sample was then weighed to determine the combined mass of the sample and corrosion products before being weighed again after removal of corrosion products using Clarke's solution. This was achieved by pipetting a thin layer of the solution onto the surface of the sample and rubbing gently with a cotton swab to remove the layer. The difference in sample mass before and after corrosion product removal was used to establish the mass of corrosion product present.

The operating conditions, test methods and analysis techniques for tests completed at the Diamond Light Source and within the University of Leeds are outlined in Table 1. Essentially, all 4 hour LPR electrochemical data and all XRD data presented in this paper were recorded at the Diamond Light Source. All other supporting electrochemical data (EIS, longer term LPR, Tafel plots) and the SEM images were collected at the University of Leeds.

Table 1. Experimental in-house laboratory tests (at the University of Leeds) and in-situ SR-XRD tests (at the Diamond Light Source Synchrotron facility).

Parameter	**In house laboratory tests for long term behaviour**	**SR-XRD tests for short term kinetics**
Material	X65 carbon steel – 9 mm Ø (exposed surface)	
Brine chemistry	3.5 wt.% NaCl, distilled water	
Solution pH	6.3, 6.8, 7	
Temperature	80 ºC	
CO_2 partial pressure	0.54 bar (1 bar total pressure in system)	
Flow velocity	0.1 m/s	
Test duration	20 hours	4 hours
Sample removal interval (ex situ analysis)	20 hours	None, but tests repeated and removed at 0.5, 1, 2, 4 hours away from beamline

In situ Electrochemical measurements	LPR, EIS, Potentiodynamic polarisation	LPR
In situ surface analysis	none	SR-XRD
Ex situ surface analysis	SEM	None, but SEM, mass gain and surface coverage analysis conducted away from beamline on removed samples at 0.5, 1, 2 and 4 hours.

3. RESULTS & DISCUSSION

3.1. Initial longer term corrosion tests and solution equilibrium chemistry

Laboratory experiments were performed over 20 hours to understand the long-term behaviour and corrosion rate transient response of X65 carbon steel as a result of changing bulk solution pH within the flow cell. These experiments formed the basis for comparison with shorter duration tests conducted over 4 hours under the exact same conditions (using an identical setup) at the Synchrotron facility. Figure 2(a) shows the Tafel plots obtained by performing separate anodic and cathodic polarisation sweeps about the OCP of X65 steel after 20 hours of immersion in the test solution. The Tafel constants (β_a = anodic Tafel constant; β_c = cathodic Tafel constant), obtained as a function of pH, were measured based on the anodic and cathodic curves in Figure 2(a) and resulted in a Stern-Geary coefficient of approximately 17 mV/decade with β_a = ~60 and β_c = ~120 mV/decade across all conditions.

Figure 2(b) shows the EIS Nyquist plots depicting the solution resistance (R_s) and the charge-transfer resistance (R_{ct}) at the start of each test on the wet-ground steel surface. The solution resistance was measured to be approximately 5 $\Omega.cm^2$ in each system.

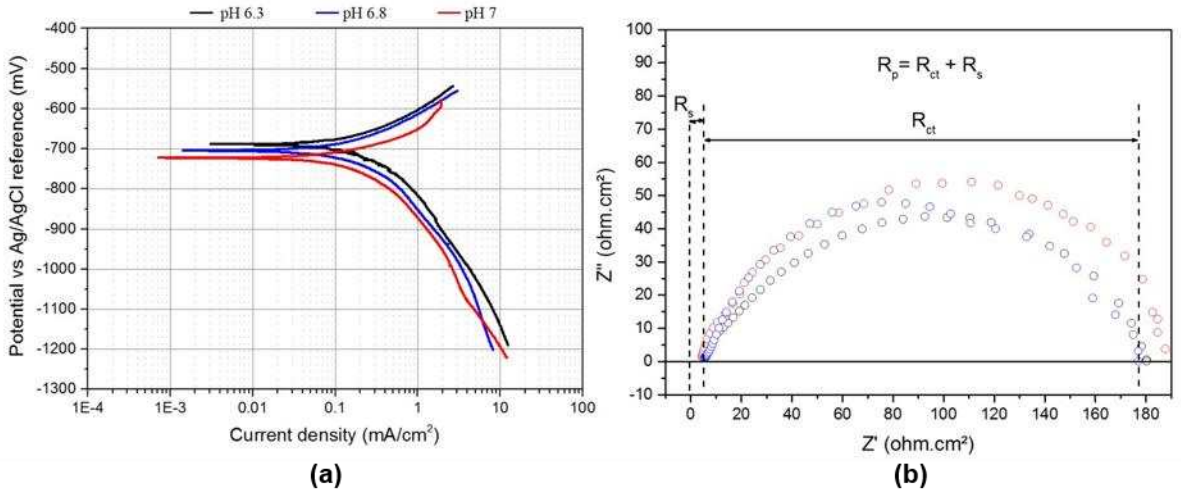

Figure 2. (a) Tafel plots and (b) EIS Nyquist plots showing the solution resistance (R_s) and the charge-transfer resistance (R_{ct}) for X65 carbon steel conducted in a CO_2-saturated 3.5 wt.% NaCl at 80°C, 0.54 bar pCO_2 and 0.1 m/s with pH values of 6.3, 6.8 and 7. Data recorded away from beamline in laboratory experiments and after 5 mins OCP stabilisation.

The effect of pH on the corrosion behaviour of carbon steel over 20 hours is shown in Figure 3. In acidic conditions, as the pH increases, the corrosivity of the solution generally decreases in CO_2 conditions due to the reduction in H^+ ions available for the cathodic hydrogen-evolution reaction. This difference can be observed in the initial stages prior to film growth in Figure 3(a), but due to the high pH of the three systems, there is only small sensitivity in initial corrosion rate to the change in pH under these conditions.

During these tests, the formation of a protective surface film at pH 6.8 and 7 lowered the corrosion rates to ~0.2 mm/year after 20 hours, whereas at the lower pH of 6.3, the final corrosion rate reached ~1.2 mm/year but was still continuing to reduce. In addition to the electrochemical observations, post-test SEM micrographs provided in Figures 3(b), (c) and (d) indicate the difference in crystal morphology for the three tests; namely the size of the crystals and their packing density. Although only marginally influencing the initial corrosion rate of carbon steel, the pH has a significant effect on the corrosion rate response with time by

influencing $FeCO_3$ formation. At higher pH, the Fe^{2+} concentration required to exceed the solubility of $FeCO_3$ is reduced, meaning saturation of the test solution is reached faster. This results in substantial levels of precipitation onto the steel surface, resulting in corrosion rates declining earlier and faster as pH increases.

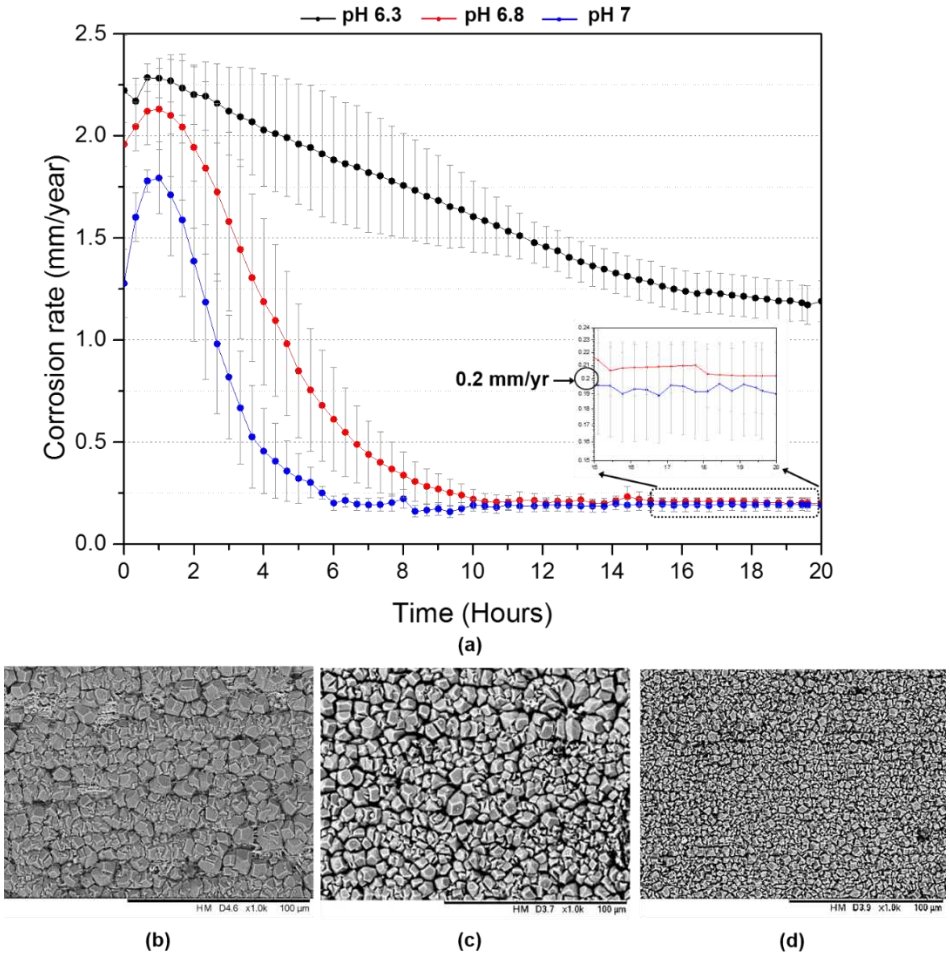

Figure 3. (a) In situ corrosion rate data over 20 hours for X65 carbon steel in a CO_2-saturated 3.5 wt.% NaCl solution at 80°C, 0.54 bar pCO_2 and 0.1 m/s with pH values of 6.3, 6.8 and 7. Data is supplemented with SEM images for (b) pH 6.3; (c) pH 6.8 and (d) pH 7 representing the surface after 20 h exposure to each condition. All data collected away from the beamline in laboratory experiments.

Through consideration of the equilibrium and dissociation reactions and their corresponding equilibrium constants (Equations (7) to (16) in Table 2) it is possible to determine the CO_3^{2-} concentration (and concentration of other ions in the system) as a function of pH in a CO_2-

saturated 3.5 w.t % NaCl solution at 80°C and 0.54 bar pCO_2. The exact equilibrium constant values included in the model are listed elsewhere (K_{sol} [23], K_{wa}[24], K_{hy}[25], K_{ca} [23], K_{ci} [23]), but the concentration of species over the pH range of 6.3 to 7 are provided in Figure 4. This figure shows that the concentration of CO_3^{2-} increases by over an order of magnitude between pH 6.3 and 7, meaning much less Fe^{2+} ions are needed to reach the critical S_{FeCO_3} required for substantial crystal nucleation and growth.

Table 2. Homogenous H_2O-CO_2 equilibrium chemical reactions and their equilibrium constants

Reaction		Equation	Equilibrium Constant	Equation
Dissolution of carbon dioxide	$CO_{2_{(g)}} \overset{K_{sol}}{\Longleftrightarrow} CO_{2_{(aq)}}$	(7)	$K_{sol} = c_{CO_2}/pCO_2$	(8)
Water dissociation	$H_2O_{(l)} \overset{K_{wa}}{\Longleftrightarrow} H^+_{(aq)} + OH^-_{(aq)}$	(9)	$K_{wa} = c_{H^+}c_{OH^-}$	(10)
Carbon dioxide hydration	$CO_{2_{(aq)}} + H_2O_{(l)} \overset{K_{hy}}{\Longleftrightarrow} H_2CO_{3_{(aq)}}$	(11)	$K_{hy} = c_{H_2CO_3}/c_{CO_2}$	(12)
Carbonic acid dissociation	$H_2CO_{3_{(aq)}} \overset{K_{ca}}{\Longleftrightarrow} H^+_{(aq)} + HCO^-_{3_{(aq)}}$	(13)	$K_{ca} = c_{H^+}c_{HCO_3^-}/c_{H_2CO_3}$	(14)
Bicarbonate anion dissociation	$HCO^-_{3_{(aq)}} \overset{K_{bi}}{\Leftrightarrow} H^+_{(aq)}) + CO^{2-}_{3_{(aq)}})$	(15)	$K_{bi} = c_{H^+}c_{CO_3^{2-}}/c_{HCO_3^-}$	(16)

To elaborate on this point further, the solubility constant (K_{sp}) shown in Equation (2) for $FeCO_3$ is determined based on the knowledge of solution temperature and ionic strength using the empirical expression proposed by Sun et al. [26] discussed previously.

$$\log K_{sp} = -59.3498 - 0.041377T_k - \frac{2.1963}{T_K} + 24.5724\log_{10}(T_K) + 2.518I^{0.5} - 0.657I \quad (17)$$

Where T_K is the temperature in degrees Kelvin (K), and I is the solution ionic strength. For a system of CO_2-saturated 3.5 wt.% NaCl at 80°C, the K_{sp} can be calculated to be 1.57×10^{-10}. Through the use of the solubility product, from Sun et al.[26] (Equation (17)) and the definition of S_{FeCO_3} in Equation (2), the Fe^{2+} concentration required for saturation of $FeCO_3$ in the bulk solution ($S_{FeCO_3} = 1$) can be determined, and this has also been included in Figure 4. Based on Figure 4 the amount of Fe^{2+} required to reach saturation is reduced by over one order of magnitude as the pH increases, due to the large increase in CO_3^{2-} concentration. The exact concentration of the species at each of the pH values considered in this paper are presented in Table 3.

Increasing solution pH has been reported to result in greater nucleation of crystals onto steel surfaces which are smaller and more densely packed. This is essentially because solution saturation can be achieved more readily at higher pH in a closed system and $FeCO_3$ nucleation increases exponentially with relative S_{FeCO_3}, whereas the rate of $FeCO_3$ crystal growth bears a linear relationship to this parameter. Therefore, nucleation dominates at high saturation while crystal growth is more influential at low S_{FeCO_3} [27]. By considering the concentrations obtained from the equilibrium model for CO_3^{2-} as a function of pH, if the same surface flux of Fe^{2+} occurs from the steel surface, then a change in pH from 6.3 to 6.8 would result in an increase in surface S_{FeCO_3} of approximately one order of magnitude, resulting in increased nucleation, but potentially less growth of crystals. Increasing pH to 7 would result in a S_{FeCO_3} 25 times higher than at pH 6.3 for the same Fe^{2+} concentration. This helps to explain the observations of increased crystal nucleation and growth with increasing pH as shown in Figure 3 (but a shift in their respective dominance). This concept will also be related to both the in situ SR-XRD and ex situ focused ion beam-scanning electron microscopy (FIB-SEM) analysis later in this paper, to explain both the crystal growth kinetics and crystal morphologies.

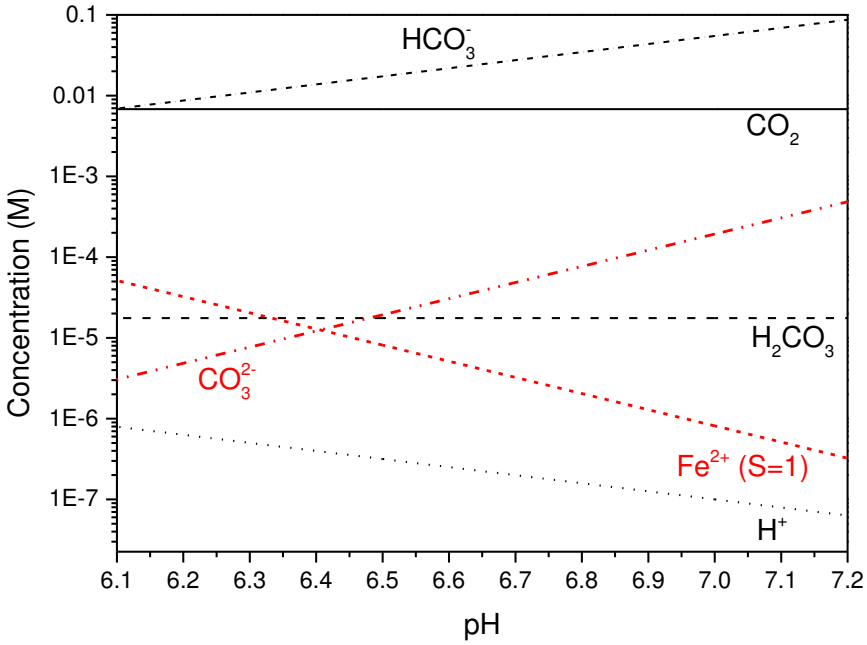

Figure 4. Equilibrium concentrations of species in the bulk solution as a function of pH in a CO_2-saturated 3.5 w.t % NaCl solution at 80°C and 0.54 bar pCO_2.

Table 3. Concentration of the species from the chemical reactions at pH 6.3, 6.8 and 7

pH	CO_2	H_2CO_3	HCO_3^-	H^+	CO_3^{2-}	Fe^{2+}
6.3	6.80 x 10^{-3}	1.76 x 10^{-5}	1.09 x 10^{-2}	5.01 x 10^{-7}	7.70 x 10^{-6}	2.04 x 10^{-5}
6.8	6.80 x 10^{-3}	1.76 x 10^{-5}	3.46 x 10^{-2}	1.58 x 10^{-7}	7.70 x 10^{-5}	2.04 x 10^{-6}
7	6.80 x 10^{-3}	1.76 x 10^{-5}	5.48 x 10^{-2}	1.00 x 10^{-7}	1.93 x 10^{-4}	8.13 x 10^{-7}

3.2. Kinetics of $FeCO_3$ film formation: *in situ* SR-XRD and *ex situ* SEM analysis

In situ SR-XRD patterns between the values 2θ=0-12° were collected continuously over 240 minutes for the three tests conducted at the Synchrotron facility. These experiments were then repeated away from the beamline for further extensive ex situ SEM analysis of the films formed over a range of time intervals between 30 and 240 minutes. The results are reviewed collectively over the following sections.

3.2.1. Composition of the corrosion products formed

Figure 5 shows XRD patterns representing the signal intensity against 2θ collected from the carbon steel surface at the end of each 240 minute experiment for the three pH values (patterns are offset for clarity).

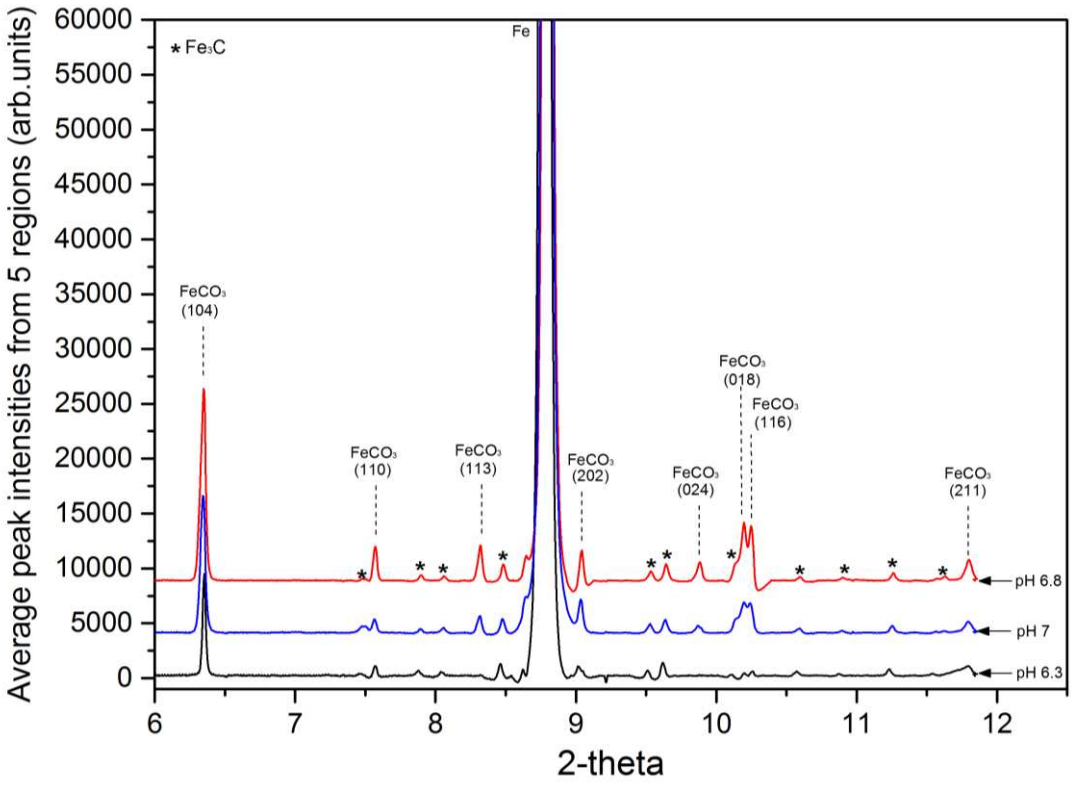

Figure 5. Selection of in situ diffraction patterns recorded from the X65 carbon steel surface within the flow cell at the Diamond Light Source beamline (I15) after 240 minutes. Test conditions were 80°C, 0.54 bar pCO_2 and 0.1 m/s in a CO_2-saturated 3.5 wt.% NaCl solution at different pH values of 6.3, 6.8 and 7. Each plot represents the average peak intensities of the phases present across a 2 mm path length at the centre of each sample which comprised of 5 individual scans. All data recorded at the Diamond Light Source powder diffraction beamline (I15).

Each pattern represents the average of five scans on the sample surface across a 2 mm linear region at the centre of each sample, performed within the space of 5 minutes. These in situ SR-XRD patterns reveal that the only crystalline phase detected on the steel surface at the end of all three experiments was $FeCO_3$. In fact, no other phases were detected at any point during the experiment, with the exception of iron carbide (Fe_3C) and iron (Fe), which already existed as

part of the steel microstructure. Among the formed $FeCO_3$ crystal planes, the most intense peak was observed at 2θ=~6.35º corresponding to the [104] plane. Given that this plane is the most dominant under all conditions, it was chosen as the main peak to correlate with the precipitation kinetics later within this work.

It is important to note here that utilising the peak intensity or peak area intensity of the (104) reflection to follow precipitation kinetics relies on the assumption that no preferred orientation of the crystals exists on the steel surface. To validate whether any preferential orientation did exist, the intensity ratios of the three most dominant peaks were compared. These three peaks correspond to the (104), (110) and (113) reflections, which should exist in peak ratios of 1:0.20:0.18, respectively. Table 4 provides the peak intensity ratios across each pH and at different time intervals. It can be observed from the table that these ratios are relatively consistent with those expected for $FeCO_3$ crystals with no preferential orientation at pH 6.3 and 6.8. Slight preferential orientation appears to exist at pH 7, but this is in favour of the (104) reflection relative to the (110) peak. It is important to take this into consideration when using such a technique to follow precipitation kinetics in a quantitative manner.

Table 4. $FeCO_3$ (104), (110) and (113) peak intensity ratios across each pH and at different time intervals

Time (min)	Average $FeCO_3$ Peak Intensities and Ratios										
	pH 6.3			pH 6.8				pH 7			
	(104)	(110)	Ratio	(104)	(110)	(113)	Ratio	(104)	(110)	(113)	Ratio
30	0	0	**0**	1399	218	190	**1:0.16:0.14**	5341	359	720	**1:0.07:0.13**
60	0	0	**0**	3767	550	624	**1:0.15:0.17**	8754	644	1133	**1:0.07:0.13**
90	0	0	**0**	7140	1072	1276	**1:0.15:0.18**	10333	709	1325	**1:0.07:0.13**
120	0	0	**0**	9366	1398	1729	**1:0.15:0.18**	11593	758	1476	**1:0.07:0.13**
150	1741	182	**1:0.1**	13321	1965	2280	**1:0.15:0.17**	12684	800	1613	**1:0.06:0.13**
180	2726	314	**1:0.12**	15417	2236	2735	**1:0.15:0.18**	12716	807	1594	**1:0.06:0.13**
210	3835	603	**1:0.16**	16023	2563	2941	**1:0.16:0.18**	12486	803	1596	**1:0.06:0.13**
240	5635	961	**1:0.17**	17080	2721	3150	**1:0.16:0.18**	12486	797	1595	**1:0.06:0.13**

3.2.3. Early stages of $FeCO_3$ film formation over time: Linking the in situ corrosion behaviour to the in situ growth kinetics

Figure 6(a) shows the in situ electrochemical corrosion measurements and Figure 6(b) shows the intensity of most dominant $FeCO_3$ (104) peak over time in the form of the average peak intensities across all five locations for the different pH values studied i.e. each point on the graph is the average intensity of the (104) peak from 5 scanned locations within the space of 5 mins. The individual responses from each of the 5 locations within all three experiments are also provided in Figure 6(c) for completeness and show the variability in the diffraction patterns observed at different locations on the same sample surface at very similar instances in time. The variability in diffraction response from the steel surface is greater at lower pH, as may be expected due to the slower kinetics resulting in larger differences in induction time on different areas of the steel surface. At the highest pH of 7, the intensity responses from each location are much more consistent with one another. However, these responses in Figure 6(c) highlight the need to sample multiple regions on the steel surface (or to have a sufficiently larger sample area) in order to obtain representative information on the induction time, nucleation and growth behaviour of corrosion products, as some non-uniformity in the growth of the film clearly exists across the surface.

In terms of relating the average intensity of the (104) peak to the corrosion response, referring back to Figure 6(a), at a starting pH of 6.3 the corrosion rate increases with time before stabilising at ~2.5 mm/year from 120 minutes onwards. In this experiment, the corrosion rate does not change throughout the remainder of the test, although interestingly, $FeCO_3$ precipitation is detected after 130 minutes as shown in Figure 6(b), reflecting the fact that the SR-XRD is capable of detecting the very early stages of crystal growth, prior to it having any substantial effect on general corrosion rate. At pH 6.8, the corrosion rate increases with time

before reducing continuously over the test duration, reaching a final corrosion rate of ~0.55 mm/year after 240 minutes.

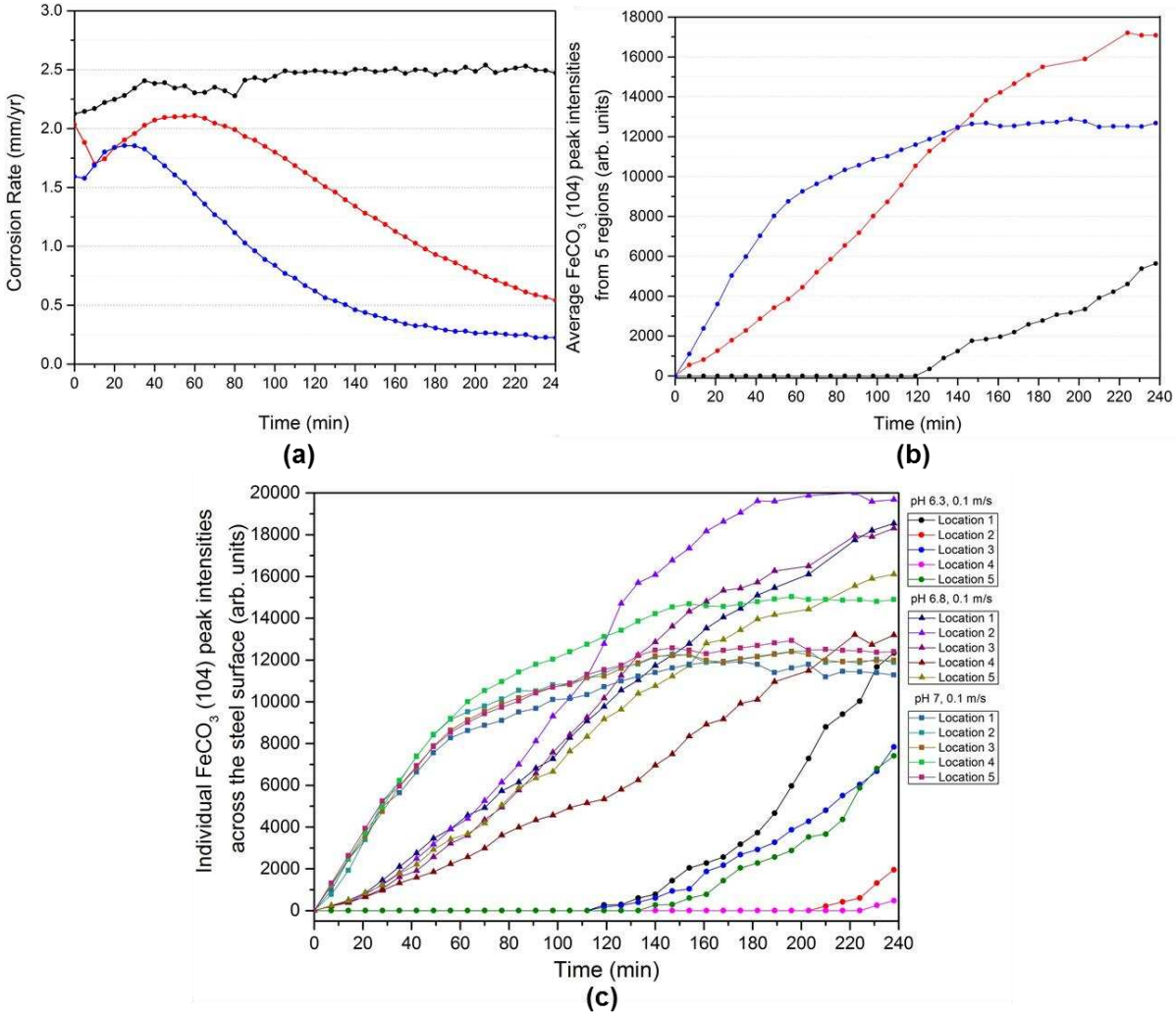

Figure 6. In situ data recorded over time at the Diamond Light Source beam line (I15) for each test conducted at 80°C, 0.54 bar pCO_2 and 0.1 m/s in a CO_2-saturated 3.5 wt.% NaCl solution at different pH values of 6.3, 6.8 and 7: (a) Corrosion rates; (b) Average $FeCO_3$ (104) peak intensities of all 5 scans performed over a 2 mm line scan on each sample; (c) Individual $FeCO_3$ (104) peak intensities of all 5 scans performed over a 2 mm line scan on each sample. All data recorded at the Diamond Light Source powder diffraction beamline (I15).

Similarly, at pH 7, the initial corrosion rate increases yet again but reduces rapidly to values of approximately ~0.2 mm/year after 240 minutes. The higher pH values of 6.8 and 7 result in higher initial surface S_{FeCO_3}, faster precipitation and formation of a more protective $FeCO_3$

film within the given timeframe due to the increase in CO_3^{2-} concentration in the bulk solution. These characteristics are reflected by a rapid decrease in the corrosion rate with time. The faster film formation at pH 6.8 and 7 observed with the in situ corrosion data is further reinforced by the in situ SR-XRD data, where it is clear from Figure 6(b) that the induction time (the time taken for the onset of crystal nucleation to occur) reduces significantly with increasing pH. The induction time of $FeCO_3$ is significantly longer at pH 6.3 (~130 minutes), compared with that at pH 6.8 and 7 (~14 and ~7 minutes, respectively), and hence the growth kinetics of $FeCO_3$ are faster at the higher pH in comparison with the system at pH 6.3, which is to be expected as the surface S_{FeCO_3} under these conditions is approximately 10 times higher at pH 6.8 and 25 times higher at pH 7 (inferred based on the similarity in surface flux of Fe^{2+} and the bulk CO_3^{2-} concentrations calculated in Table 3).

When comparing the two systems operating at pH 6.8 and 7, assuming a direct relationship between crystal growth kinetics and peak intensity transient response extracted from the XRD patterns, the growth kinetics are noticeably different. The initial nucleation and crystal growth rate is faster at pH 7, but the primary difference is that the growth rate decreases until a plateau is approached after ~125 minutes (blue plot in Figure 6(b)) and remains constant until the end of the experiment. Here, the crystal growth rate decreases due to larger proportions of the surface being covered with crystals and ultimately reducing the production of Fe^{2+} from the steel surface, which has a direct impact on the formation of $FeCO_3$, reducing the precipitation rate. These observations are consistent with the trend in electrochemical data. In comparison, at a pH of 6.8, the induction time for $FeCO_3$ nucleation is also comparatively fast (< 14 mins), but the crystal growth rate is relatively constant throughout the majority of the experiment, slowing down towards the final hour. Importantly, the peak intensity at the end of the experiment at pH 7 is lower than the experiment at pH 6.8, indicating that the film formed at the higher pH is thinner and/or has less mass, yet offers more protection to the steel substrate.

SEM images later in this paper indicate that very high surface coverage of $FeCO_3$ crystals is achieved at both pH 6.8 and 7 after 4 hours, and that the key difference for the higher intensity measured at pH 6.8 after 4 hours is the difference in thickness of the corrosion product film. This difference in film thickness is highlighted in Figures 7(a-h) which are SEM images where a focused ion beam (FIB) has been used to mill a cross-section into the protective $FeCO_3$ film to reveal the layer thickness.

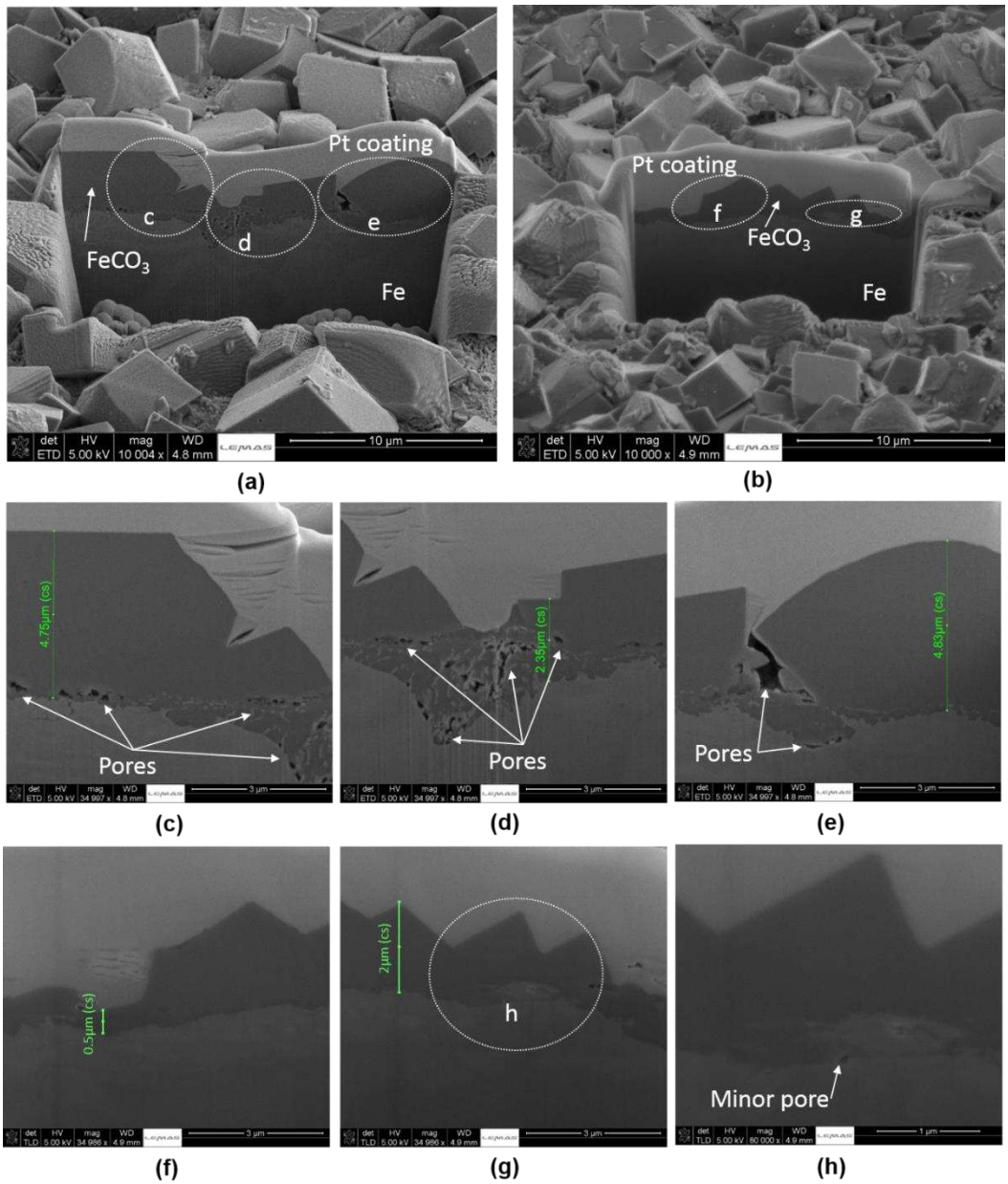

Figure 7. Ex situ SEM images of the X65 carbon steel surface at the end of the 4 h Synchrotron test showing the cross-sections of the films formed at the end of the synchrotron

tests (80°C, CO_2-saturated 3.5 wt.% NaCl solution at 0.54 bar pCO_2 and 0.1 m/s) at (a)/(c-e) pH 6.8 and (b)/(f-h) pH 7.

Figure 7(a) and (c-e) shows the area removed, revealing the cross-section of the $FeCO_3$ film formed at pH 6.8. The film ranges from 2 to 4.75 μm in thickness. Figures 7(c-e) also show the presence of pores at the steel and $FeCO_3$ crystal interfaces, allowing a pathway for species to diffuse to and from the steel surface. These pores are not detectable from the top view SEM images.

Figures 7(b) and (f-h) show the area milled away revealing the cross section of the $FeCO_3$ film formed at pH 7. The film ranges from 0.5 to 2 μm in thickness. Unlike the crystals formed at pH 6.8, Figures 7(f-h) show crystals that are better adhered to the steel surface interface which more effectively block the surface reaction and diffusion of species to and from the surface. The images show that the film formed at pH 6.8 is considerably thicker and consists of much larger crystals than those at pH 7, agreeing with the measured XRD peak intensities (i.e. higher intensity was observed for the thicker film at pH 6.8 after 4 hours). As a final point in Figure 7, there is a clear difference in the level of compactness of crystal and their interaction with the substrate. Crystals formed at pH 7 produced a less porous layer which conforms better to the steel substrate compared to crystals precipitated at pH 6.8, which aids in explaining why corrosion rates were noticeably lower after 4 hours at pH 7.

3.2.2. Early stages of $FeCO_3$ film formation over time: Development of film through ex situ SEM observations

Theoretically, the peak area for a specific crystal plane in a diffraction pattern is proportional to the crystal volume (or mass if a fixed density is assumed). Therefore, evaluating the average peak area intensity as a function of time provides a suitable technique to follow the evolution of $FeCO_3$ formation kinetics in real-time.

In this section, in situ SR-XRD and corrosion rate measurements are compared with ex situ SEM observations showing the visual appearance of the corroding steel surface and $FeCO_3$ crystals developing over time. Figures 8(a-e), 9(a-e) and 10(a-e) relate to the three different pH values of 6.3, 6.8 and 7, respectively. The SEM images depicting the morphology and extent of precipitation of $FeCO_3$ crystals onto X65 carbon steel surfaces was conducted by running numerous experiments at different durations of 30, 60, 120 and 240 minutes away from the beamline. The ex situ SEM images enable determination of the structure and morphology, size and the amount of the surface occupied by the crystals at each pH over time, which can be correlated with specific data from the XRD patterns collected. The SEM images within the figures are analysed at a magnification of x3000 to project an area of ~70x70 µm to represent the size of the beam and to illustrate the area of the surface being scanned at each location. Additionally, Figures 8(e), 9(e) and 10(e) shows the kinetics of the $FeCO_3$ crystal growth in the form of the average peak area intensity from all five locations which can be compared with the electrochemical response that provides an average corrosion rate over the steel surface.

Figure 8 refers to the kinetics of $FeCO_3$ formation for pH 6.3. In Figures 8(a) and (b), no crystals are observed until 120 minutes (Figure 8 (c)) which agrees with the observed $FeCO_3$ intensity increase in Figure 8(e). At this point, it can be assumed that the system has reached the critical S_{FeCO_3} required for not only $FeCO_3$ nucleation but also further crystal growth because in the following 120 minutes, the $FeCO_3$ intensity rapidly increases and more crystals are captured in Figure 8(d) with a slight increase in overall size to ~1.5 µm, covering approximately 23% of the surface. An interesting observation here is that despite the growth of $FeCO_3$ crystals on the surface, the corrosion rate remains stable at 2.4 mm/year with only a small indication of a potential decrease after 230 minutes. Although $FeCO_3$ crystals are present, at this point in time they offer minimal protection to the steel surface against corrosion.

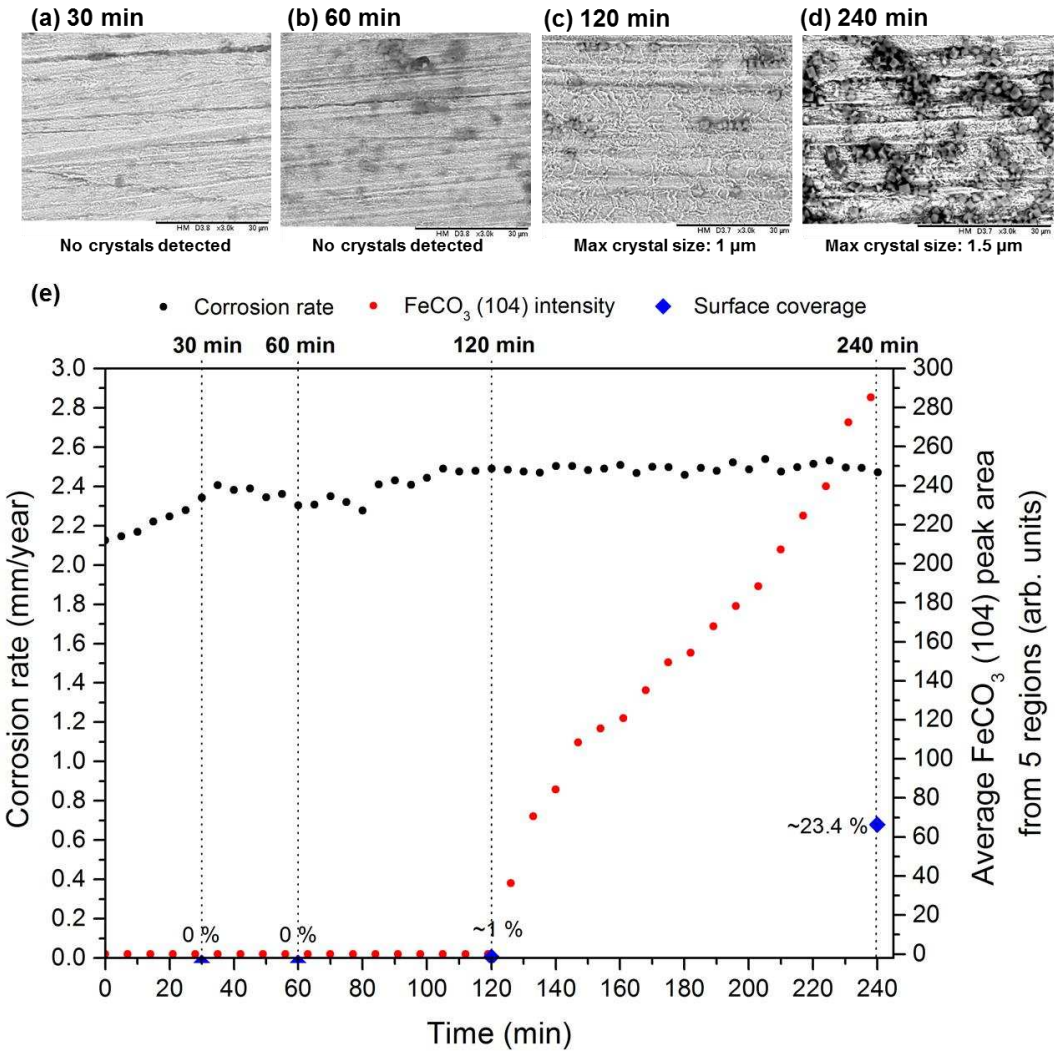

Figure 8. Development of the $FeCO_3$ crystals; (a)-(d) SEM images as a function of time (scale bar corresponds to 30 µm and data collected from laboratory repeats); (e) In situ corrosion rate and major $FeCO_3$ (104) average peak area versus time collected at beamline I15, conducted in a CO_2-saturated 3.5 wt.% NaCl solution at 80°C, 0.54 bar pCO_2 and 0.1 m/s at pH 6.3.

In comparison to the previous test conducted at pH 6.3, the decrease in Fe^{2+} solubility as a result of increased bulk solution pH to 6.8 has enhanced both the nucleation and growth rate of $FeCO_3$ crystals which is evident from Figure 9(e). SEM images of the X65 steel surface after exposure to the solution at pH 6.8 for 30, 60, 120, and 240 minutes are provided in Figure 9 (a-d).

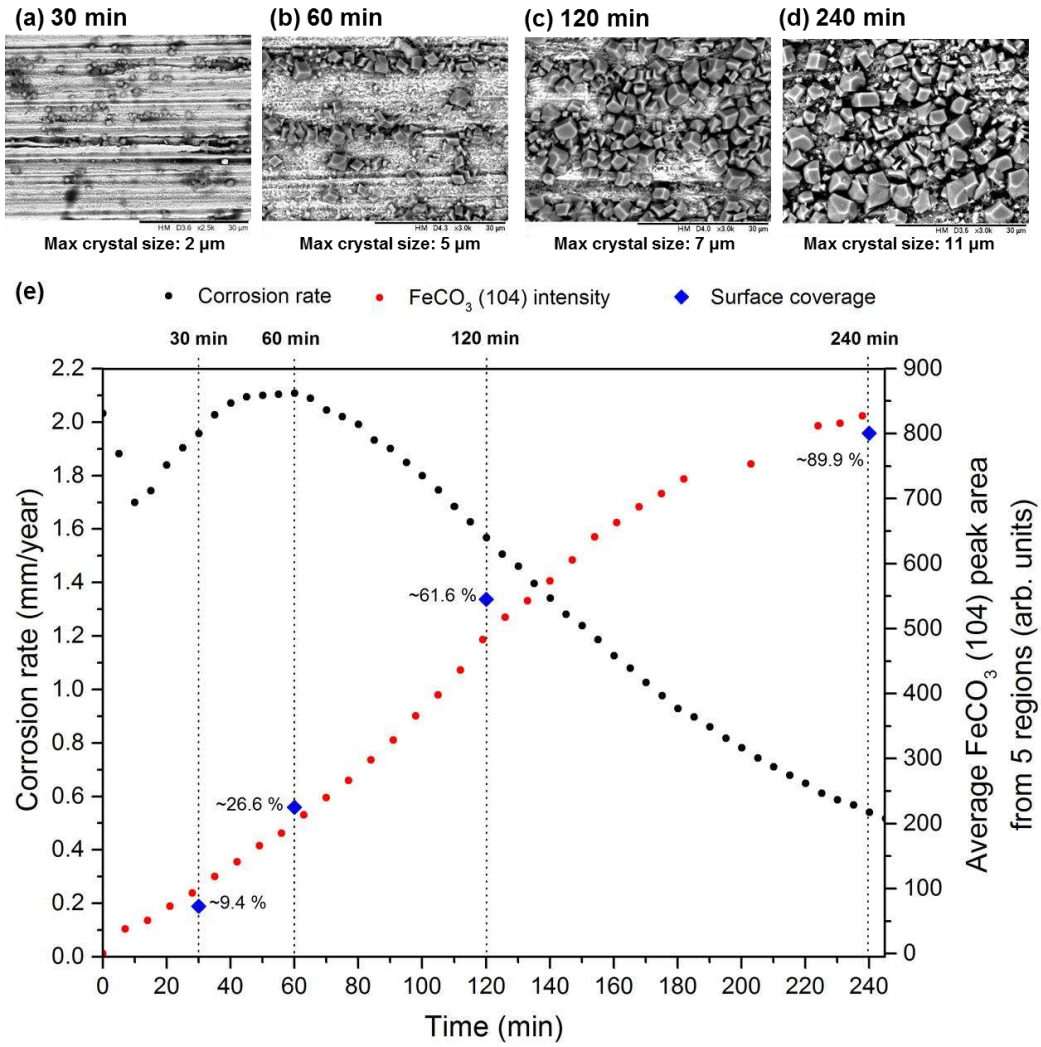

Figure 9. Development of the $FeCO_3$ crystals; (a)-(d) SEM images as a function of time (scale bar corresponds to 30 µm and data collected from laboratory repeats); (e) In situ corrosion rate and major $FeCO_3$ (104) average peak area versus time collected at beamline I15, conducted in a CO_2-saturated 3.5 wt.% NaCl solution at 80°C, 0.54 bar pCO_2 and 0.1 m/s at pH 6.8.

After 30 minutes, following nucleation, discrete crystals on the surface begin to grow with crystal sizes varying from <1 µm to 2 µm in width (Figure 9(a)) covering ~9.4% of the surface. At this stage the crystals offer little or no protection against corrosion. After 60 minutes, the nucleated crystals have grown, with an average size from 1 µm to 5 µm in width (Figure 9(b)) whilst new crystals continue to nucleate on to the steel surface. In conjunction with this behaviour, the corrosion rate begins to decrease as a result of the $FeCO_3$ crystals blocking active sites on the steel surface with ~26.6% of the surface covered with $FeCO_3$. From 60 minutes onwards, the combined in situ observations and ex situ SEM images exemplify that this process

of nucleation and growth continues until the $FeCO_3$ film has the ability to reduce the corrosion rate significantly. This sequence of nucleation and growth illustrates that as the $FeCO_3$ layer develops, larger proportions of the surface are being covered with crystals, ultimately reducing the access of electrochemically active species to the surface, but also limiting the surface flux of Fe^{2+} from the steel surface, which has a direct impact on the formation of $FeCO_3$, reducing the precipitation rate. Therefore, as the $FeCO_3$ layer builds up, the precipitation kinetics slow down which is captured by the SR-XRD measurements after 175 minutes in Figure 9(e). After 240 minutes, further nucleation and growth then contributes to a subsequent build-up of the $FeCO_3$ layer with crystals ranging from 1 μm to 10 μm. By the end of the experiment, areas still exist on the steel surface through which the electrolyte has a direct pathway to the steel surface, allowing the steel to continue to corrode at a reduced rate of ~0.6 mm/year.

A further increase in system pH to 7 resulted in even more substantial levels of $FeCO_3$ precipitation occurring earlier in the experiment with increased nucleation as seen in Figure 10. This was attributed to the solubility of Fe^{2+} being further reduced due to the increased pH. No significant change in the morphology of the film was observed between this test and the previous test (pH 6.8) other than the size of $FeCO_3$ crystals with sharper and more defined edges (Figure 10 (a)-(d)).

After just 30 minutes of exposure (Figure 10(a)), a significant proportion of the steel surface was covered by small $FeCO_3$ crystals varying from <1 μm to 2 μm in width that possessed a very similar structure to those observed at pH 6.8. After just 60 minutes of exposure, ~50% of the surface is covered with $FeCO_3$ crystals which is observed in Figure 10(b). In conjunction with these observations, the corrosion rate is rapidly reducing at this stage. After 120 minutes of exposure, a very large portion of the surface was covered by $FeCO_3$ crystals varying from 1 μm to 5 μm in width. At this point, the rate of reduction in corrosion rate (Figure 10(e)) has

slowed down due to the reduction in Fe^{2+} production from the surface, hindering $FeCO_3$ formation.

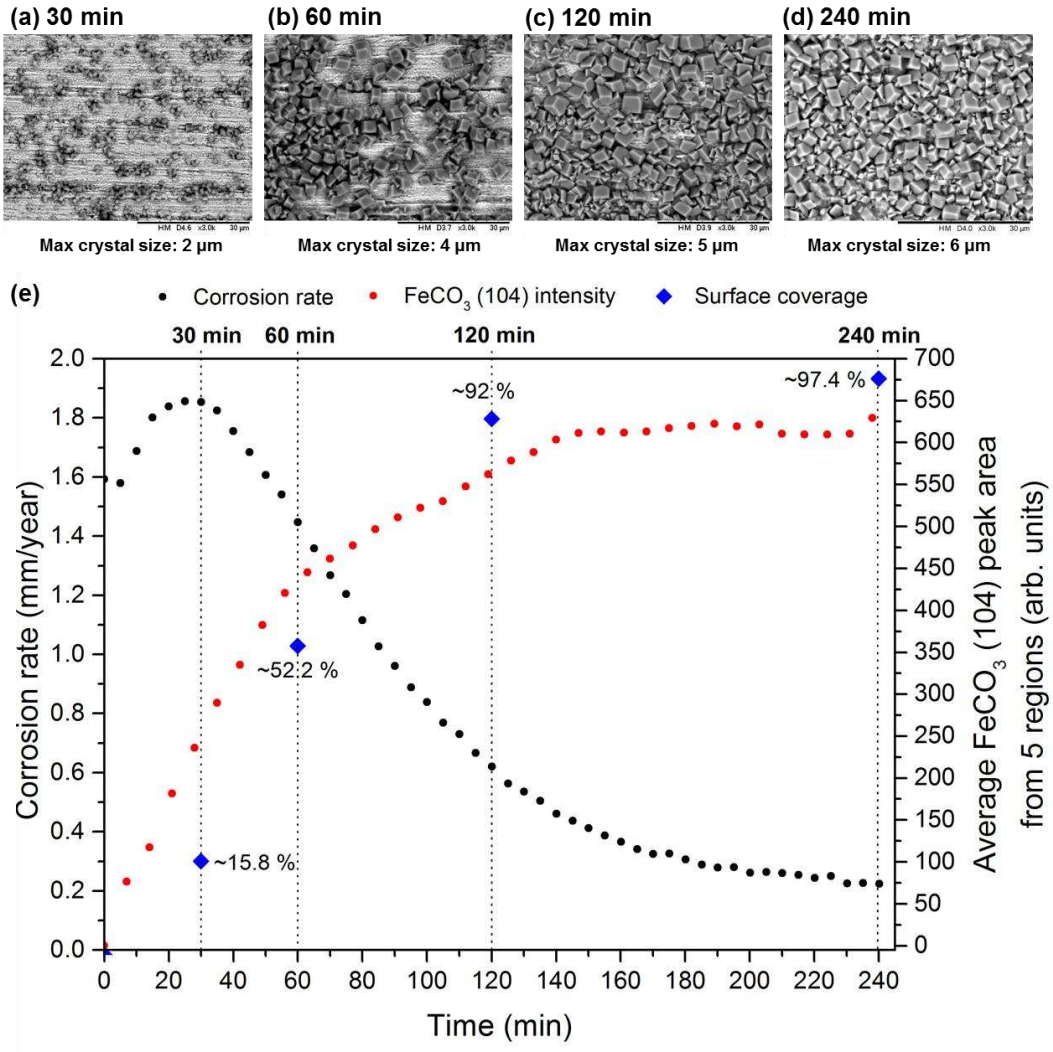

Figure 10. Development of the $FeCO_3$ crystals; (a)-(d) SEM images as a function of time (scale bar corresponds to 30 µm and data collected from laboratory repeats); (e) In situ corrosion rate and major $FeCO_3$ (104) average peak area versus time collected at beamline I15, conducted in a CO_2-saturated 3.5 wt.% NaCl solution at 80°C, 0.54 bar pCO_2 and 0.1 m/s at pH 7.

The corrosion rate gradually continues to drop until the end of the test were almost entire surface coverage is achieved. Very few changes were observed from the SEM images from 120 minutes onward with the only noticeable difference being a minor increase in crystal size. Comparing this to the previous test, the maximum crystal size here is almost half the size of the largest crystal found at pH 6.8 through SEM observations. It has to be noted that the surface

coverage at pH 7 continued to increase marginally even though a plateau in $FeCO_3$ intensity occurred. This may be due to the fact that precipitation was limited at this stage and that the regions scanned by XRD were already fully covered, producing no variation in intensity and a slight mismatch between the in situ and ex situ observations. Figure 11 summarises the effect of pH on the development and morphology of the $FeCO_3$ crystals over time.

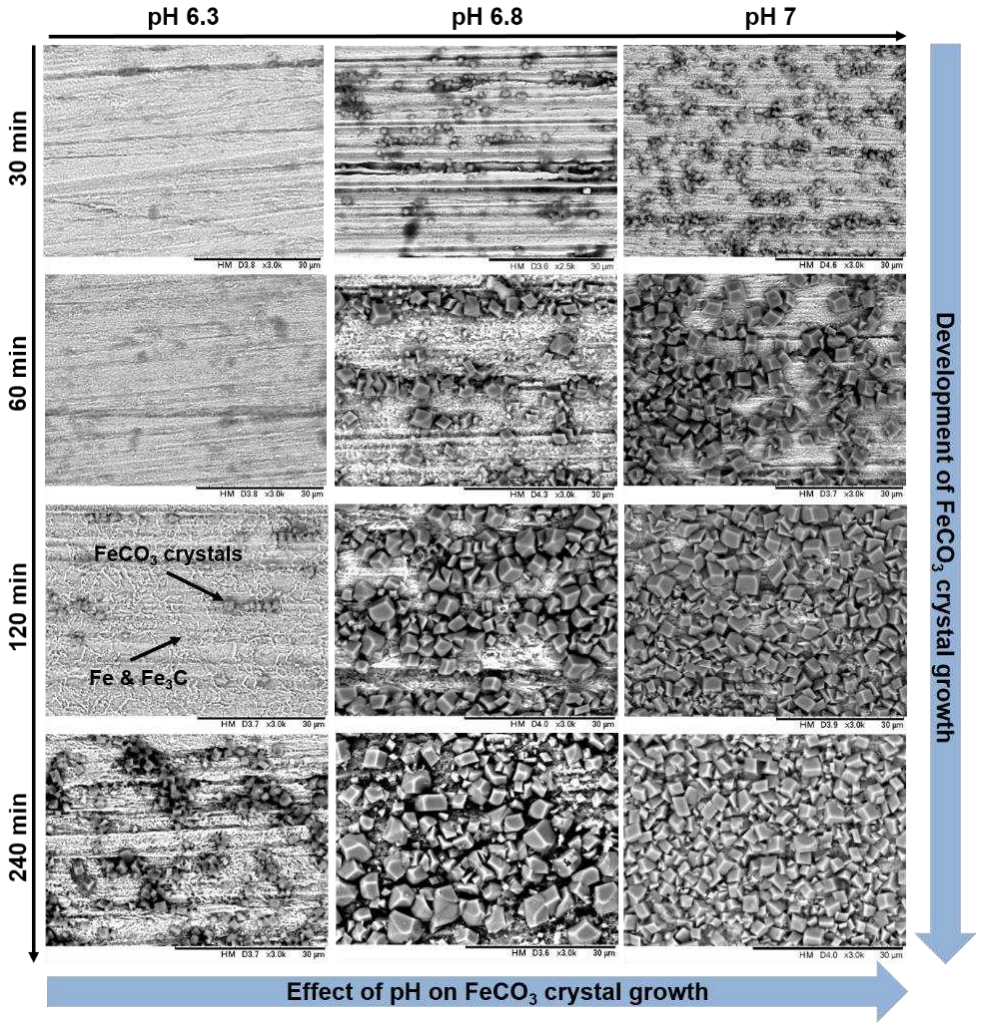

Figure 11. The effect of pH on the development and morphology of $FeCO_3$ crystals over time conducted in a CO_2-saturated 3.5 wt.% NaCl solution at 80°C, 0.54 bar pCO_2 and 0.1 m/s at pH values of 6.3, 6.8 and 7.

The main differences throughout the tests at each pH were the sizes and growth rate of the crystals. The crystals formed at pH 7 appear to have sharper and more defined edges, whereas at pH 6.8, the crystals on the surface appear to be a mixture of well-defined cubic crystals with

sharp edges (as seen at pH 7). The crystals at pH 6.8 also seem to vary in size considerably in comparison to the $FeCO_3$ at pH 7. It is well documented that the increase in pH significantly decreases the solubility of Fe^{2+}, resulting in faster precipitation and hence increased rate of surface coverage. Consequently, $FeCO_3$ precipitation is far more favourable at the higher pH and has resulted in the formation of a smaller, compact and more protective crystals covering larger portions of the steel surface. These observations link back to the nucleation and growth theory when discussing long term corrosion behaviour in the previous sections.

3.3. Mechanism of $FeCO_3$ film formation

In practice, the process of $FeCO_3$ nucleation is observed more typically in the presence of impurity particles and foreign surfaces (heterogeneous nucleation)[28]. The $FeCO_3$ precipitation process in this context starts with heterogeneous nucleation, a process which is capable of occurring easily due to the numerous imperfections and adsorption sites to develop $FeCO_3$ [8]. Nucleation is then followed by the crystal growth process which essentially limits the rate of overall precipitation.

The key role of S_{FeCO_3} in $FeCO_3$ formation has long been identified, initially by Dugstad [27]. The importance of the S_{FeCO_3} near the steel surface was also discussed by Nesic and Lee [29]. Moreover, research efforts have also been directed towards understanding the role of nucleation and crystal growth according to the saturation level of $FeCO_3$ close to the steel surface by Gao et al [30]. In the context of this work, the initial S_{FeCO_3} at the corroding surfaces are orders of magnitude different from pH 6.3 to pH 7, leading not only to very different nucleation and growth rates, but differences in relative dominance between the two processes.

With consideration of in situ electrochemical, in situ SR-XRD and ex situ SEM data combined, it can be interpreted that the formation of the $FeCO_3$ crystals have caused the decline in corrosion rate in the tests performed in this work. It is proposed that the initial increase in

corrosion rate generated a high near-surface concentration of Fe^{2+}. A combination of surface roughening through the corrosion of the sample and high local S_{FeCO_3} (especially at the higher pH), will have promoted the significant heterogeneous nucleation of $FeCO_3$ crystals on to the steel surface. The combined in situ observations and ex situ SEM images illustrate that the process of nucleation and growth continues until the $FeCO_3$ film is protective enough to reduce the corrosion rate significantly. However, this sequence of nucleation and growth illustrates that as the $FeCO_3$ layer develops, larger proportions of the surface are being covered with crystals and ultimately reducing the reaction rate of Fe^{2+} production across the surface which has a direct impact on the formation of $FeCO_3$, reducing the precipitation rate and limiting $FeCO_3$ precipitation. Therefore, as the $FeCO_3$ layer builds up, the $FeCO_3$ growth rate kinetics slow down which is captured by the SR-XRD measurements. From the accumulated measured peak areas and intensities from the tests, four steps characterise the growth mechanism of the $FeCO_3$ layer. During each step, either the nucleation rate or the crystal growth rate dominates the kinetics of the layer build up. The steps, based on the work in this paper are characterised as followed:

(1) An induction time when the measured $FeCO_3$ intensity is zero and no nucleation or crystal growth rate occurs (high Fe^{2+} production rate and therefore higher S_{FeCO_3});

(2) Nucleation of the $FeCO_3$ crystals when the measured intensity (of $FeCO_3$) starts to increase (nucleation rate dominates as new crystals initially form). At this point, the production of Fe^{2+} is still rising (high S_{FeCO_3});

(3) Nucleation-growth stage which is characterised by an increase in crystal growth, but also the nucleation and growth of new crystals. Here, the Fe^{2+} production rate will begin reduce at some time along with the relative S_{FeCO_3}, whilst crystals continue to grow;

(4) Growth stage when the integrated intensity of $FeCO_3$ slows down or reaches a plateau (crystal growth dominates the kinetics due to formation of a protective $FeCO_3$ film and

hence a reduction in S_{FeCO_3} and Fe^{2+} production, while nucleation of new crystals reduces). Larger $FeCO_3$ crystals are present on the surface.

A schematic representation of the different steps of $FeCO_3$ crystal growth mechanism is provided in Figure 12.

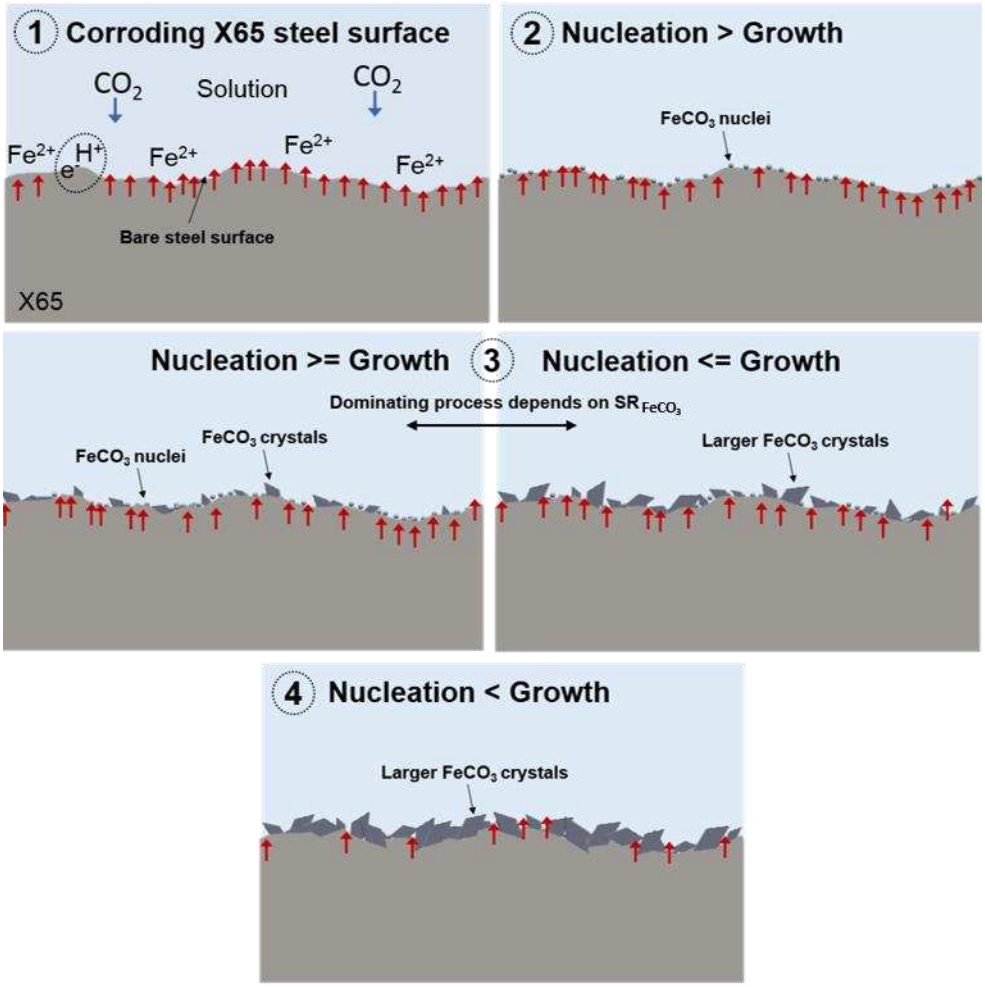

Figure 12. Schematic diagram showing the different steps of $FeCO_3$ crystal growth mechanism (red arrows indicating pathways for anions/cations to and from the bulk solution/steel surface).

As mentioned previously, the nucleation rate is believed to increase exponentially with the relative S_{FeCO_3}, whilst the crystal growth rate varies linearly[27]. When the relative S_{FeCO_3} is high, nucleation dominates and a nano-crystalline or even amorphous film can develop [19, 31]. Conversely, crystal growth should play a more substantial role at lower relative S_{FeCO_3}. This work has illustrated that increasing pH results in an increase in initial surface S_{FeCO_3} for the

same surface flux of Fe^{2+} which results in the increased nucleation and overall faster precipitation of $FeCO_3$ which is evident from the ex situ SEM and the in situ SR-XRD data presented.

3.4. Use of *in-situ* SR-XRD for quantitative and qualitative analysis of precipitation kinetics and surface coverage

A particular focus of this study was to identify whether a quantitative link could be established between the intensity of the in situ SR-XRD patterns and the mass of $FeCO_3$ on the steel surface. As stated previously, the peak area intensity for a specific crystal plane in a diffraction pattern is proportional to the crystal volume. For a fixed crystal density, this relationship should hold for the mass of $FeCO_3$ on the steel surface.

Accurately quantifying the kinetics of $FeCO_3$ and other corrosion products (such as iron sulphide) on the internal walls of carbon steel pipeline is of huge importance to the oil and gas industry and has been the subject of significant research attention in recent years. The ability to monitor film precipitation kinetics in real time and relate this to the protectiveness of the various films capable of forming on the steel surface enables more robust corrosion management strategies and corrosion prediction tools/models to be developed which account for the presence of such films.

A vast amount of research has been conducted focusing on evaluating precipitation kinetics of corrosion products in oilfield environments, particularly in terms of $FeCO_3$. However, the main challenges in determining precipitation kinetics of $FeCO_3$ relate to the suitability and accuracy of the methodologies applied to determine growth rates. For example, previous studies by Johnson and Thomson [32] and Greenberg and Thomson [33] have typically involved inferring precipitation rates through the measurement of Fe^{2+} ion concentration drop within the bulk solution. Based on this methodology, the assumption is made that all precipitation in the system occurs on the steel surface, something which was shown to be invalid through work performed

by Sun and Nesic [28]. In fact, Sun and Nesic [28] showed that the original models developed for $FeCO_3$ precipitation overestimated film growth by orders of magnitude. Such conclusion were based on result obtained using the 'weight gain' method in which the sample is weighed before and after removal of the corrosion product through the use of Clarke solution. Although this method was shown to be much more robust and to provide a more accurate measurement of $FeCO_3$ precipitation rates, the approach (just as with mass loss measurement) provides an integral value over a particular time frame. Hence, as well as being time consuming, the approach does not provide real-time precipitation kinetics and measurements of small mass gains can be challenging.

Consequently, from this study the interest was in examining if there was a relationship between film mass and average peak area intensity from the produced diffraction patterns across all five scanned regions. However, although using in situ SR-XRD theoretically is an ideal means of determining the growth kinetics and composition of corrosion products in conjunction with the electrochemical behaviour, the measurement of such small crystal masses to correlate with the peak intensities is challenging and proved impractical for the very early stages of film growth in each of the tests conducted. This was mostly attributed to the small sample size required to minimise water path length through the flow cell. As a result of this, only the final mass of corrosion products could be correlated with the XRD patterns with any certainty. Figure 13 shows the relationship between the mass of the corrosion product film on the steel surface with the average peak area intensity and total $FeCO_3$ calculated volume (calculated using surface coverage and average crystal size) under each pH condition.

Based on this figure, there is evidence to suggest that the technique may hold promise in terms of providing quantitative analysis of film mass for a fixed incident angle and a calibrated system. To achieve a better understanding of capabilities of SR-XRD to infer precipitation

kinetics and overcome limitations of being able measure earlier levels of mass gain, the surface coverage extracted from multiple SEM images was correlated with average peak area intensity.

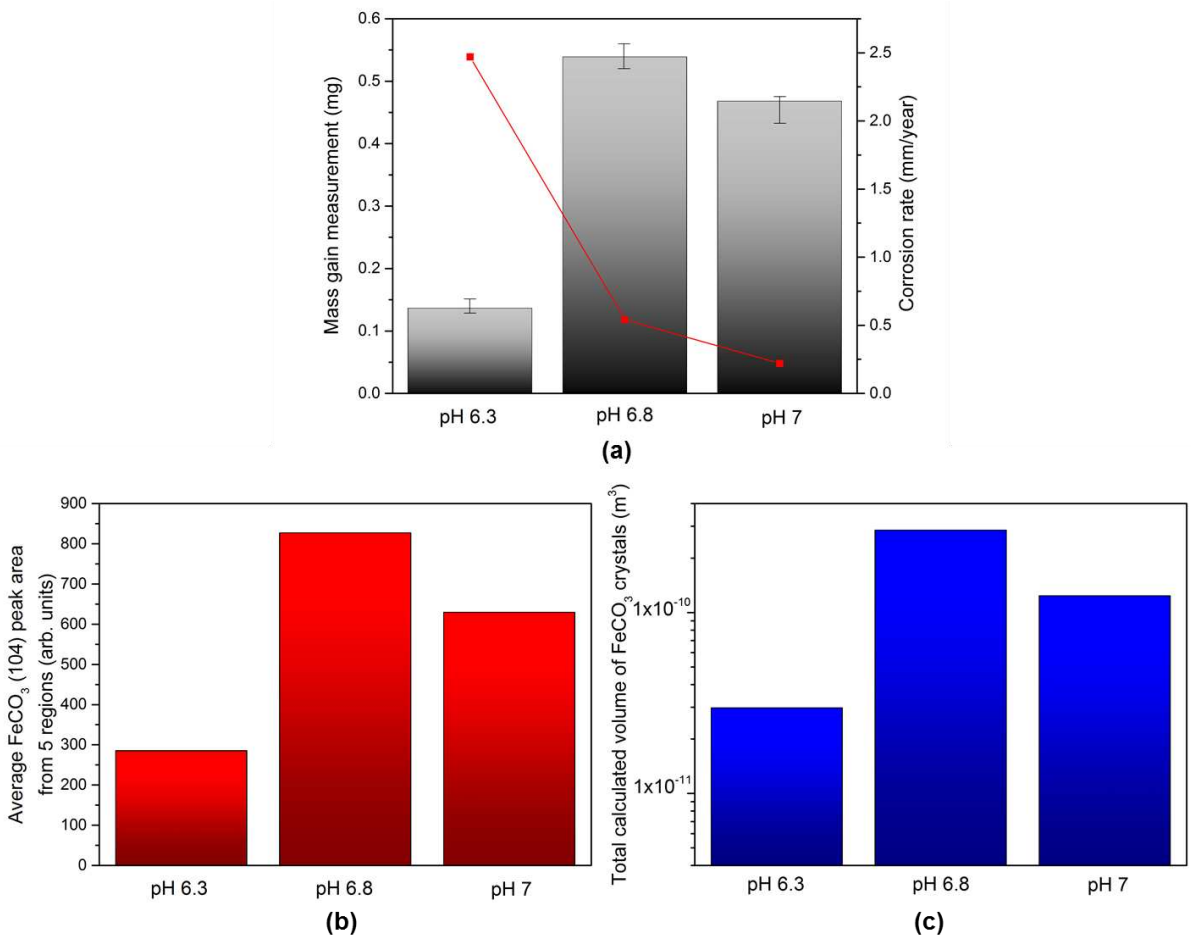

Figure 13. Relationship between (a) the mass of the corrosion product film on the steel surface with (b) the average $FeCO_3$ (104) peak area at the end of the tests and (c) total calculated $FeCO_3$ volume on the steel surface.

Although a direct comparison across all pH values could not be performed due to different film thicknesses, it would be possible to see if the peak area intensity correlated with the quantity of film for each individual pH separately as more of the surface became occupied by crystals. Considering that the spot size scanned on the surface was significantly greater than thickness of the film (i.e. five 70 x 70 µm scanned areas vs. a <5 µm thick film), it would be expected that a good correlation could be achieved between the two values, particularly at higher levels of surface coverage. However, accurate correlation does require the assumption that the regions

where film growth is present is relatively consistent in thickness and that these distinct areas have the same mass density.

Figure 14 shows the correlation between surface coverage and average peak area intensity over five different scanned areas of the steel surface. Considering the small areas processed from images and SR-XRD, the agreement is very strong. Again, these observations reinforce the capability of SR-XRD to help understand and quantify precipitation kinetics. At the very least, these results indicate that SR-XRD and processing of the (104) peak intensity can provide qualitative data on the film growth kinetics, but strong potential exists to develop this into a quantitative technique.

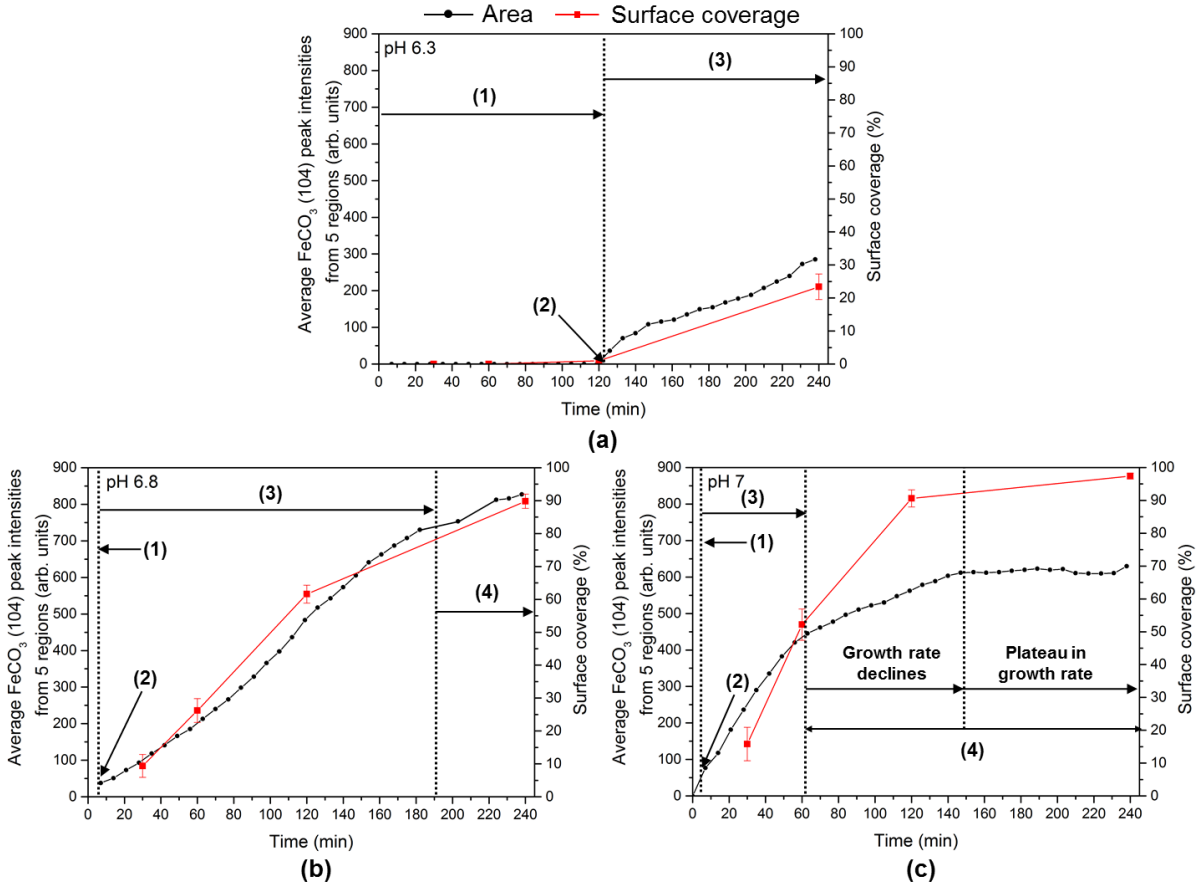

Figure 14. In situ average $FeCO_3$ (104) plane peak area compared with the surface coverage for each test showing the different steps of $FeCO_3$ crystal growth mechanism: (a) pH 6.3; (b) pH 6.8 and (c) pH 7.

4. CONCLUSIONS

A new system comprising of a flow cell with integrated in situ electrochemistry and SR-XRD capabilities has been used to follow the steel dissolution and $FeCO_3$ precipitation kinetics of X65 carbon steel in real-time in a CO_2-saturated brine at different pH values of 6.3, 6.8, and 7 when subjected to a flow rate of 0.1 m/s. The following conclusions can be extracted from the results presented in this work:

- $FeCO_3$ nucleation could be detected consistently and well before its inhibitive effect on general corrosion rate was recorded from electrochemical responses, indicating that in situ SR-GXRD is able to detect the very early stages of crystal nucleation on surfaces in a flowing cell.
- Under the specific conditions evaluated, $FeCO_3$ was the only crystalline phase to form in the system, with no crystalline precursors being apparent prior to or during its formation and being the sole phase responsible for the observed reduction in corrosion rate, predominantly through the blocking of active sites on the steel surface.
- The growth and the morphology of the $FeCO_3$ crystals recorded using in-situ diffraction patterns can be well described by the most dominant [104] crystal plane which is the most predominant during the nucleation and growth of $FeCO_3$.
- From the response of the average peak intensities and peak area intensities collected from diffraction patterns for the [104] plane as a function of time from multiple surface locations, four steps characterised the growth mechanism of the $FeCO_3$ layer: (1) An induction time when the measured intensity is zero; (2) Nucleation of the $FeCO_3$ crystals when the measured intensity initially increases; (3) Nucleation-growth stage which is characterised by an increase in crystal growth with nucleation occurring simultaneously; (4) Growth stage when the integrated intensity slows down and near full surface coverage is achieved, limiting nucleation.

- The induction time for $FeCO_3$ formation significantly reduces with increased pH, which also causes increase in crystal nucleation rate resulting in the formation of a smaller, compact and more protective crystals in the early stages of growth.
- There was insufficient evidence to show in situ SR-XRD measurements allow a complete quantification of the mass or thickness of the film formed on the steel surface. However, comparisons between crystal mass, surface coverage and peak area (integrated intensity) of the (104) reflection demonstrates a strong agreement to provide robust qualitative data on precipitation kinetics. Results also suggested that quantitative information on mass gain or precipitation kinetics could be achieved with the use of a constant incidence angle on a calibrated system.
- The results clearly indicated that the quantity of $FeCO_3$ (in terms of mass, thickness and measured intensity) on the steel surface is not necessarily a good indication of the protectiveness of the film formed. This highlights the importance of combined diffraction and electrochemical measurements in understanding film formation processes which may influence corrosion management strategies in the oil and gas industry.

ACKNOWLEDGMENTS

The authors would like to thank the Diamond Light Source for beam time (Beamline I15, reference EE12481-1), specifically Dr Annette Kleppe and Allan Ross for assistance before and during our visit. We would also like to thank Steve Caddick, Graham Brown and Mick Huggan for their expertise and assistance with the design and manufacture of the flow cell. Lastly we would like to thank BP for their financial support throughout this project.

REFERENCES

1. Han, J., S. Nesic, Y. Yang, and B.N. Brown, Spontaneous passivation observations during scale formation on mild steel in CO_2 brines. Electrochimica Acta, 2011. **56**(15): p. 5396-5404.
2. Hassani, S., K.P. Roberts, S.A. Shirazi, J.R. Shadley, E.F. Rybicki, and C. Joia, Flow Loop Study of NaCl Concentration Effect on Erosion, Corrosion, and Erosion-Corrosion of Carbon Steel in CO_2-Saturated Systems. CORROSION, 2012. **68**(2): p. 026001-1-026001-9.
3. Hua, Y., R. Barker, T. Charpentier, M. Ward, and A. Neville, Relating iron carbonate morphology to corrosion characteristics for water-saturated supercritical CO_2 systems. The Journal of Supercritical Fluids, 2015. **98**: p. 183-193.
4. Barker, R., Y. Hua, and A. Neville, Internal corrosion of carbon steel pipelines for dense-phase CO_2 transport in carbon capture and storage (CCS)–a review. International Materials Reviews, 2017. **62**(1): p. 1-31.
5. Dugstad, A., L. Lunde, and S. Nesic. Control of internal corrosion in multi-phase oil and gas pipelines. in Proceedings of the conference Prevention of Pipeline Corrosion, Gulf Publishing Co. 1994.
6. Garside, J. Advances in the characterization of crystal growth. in AIChE symposium series. American institute of chemical engineers, 1984. **80**(240): p. 23-38.
7. Kermani, M. and A. Morshed, Carbon Dioxide Corrosion in Oil and Gas Production - A Compendium. Corrosion, 2003. **59**(8): p. 659-683.
8. Meenan, P., From Molecules to Crystallizers: An Introduction to Crystallization Crystal Growth & Design, 2001. **1**(1): p. 101-101.
9. Guo, S., L. Xu, L. Zhang, W. Chang, and M. Lu, Corrosion of Alloy Steels Containing 2% Chromium in CO_2 Environments. Corrosion Science, 2012. **63**: p. 246-258.
10. Nesic, S., Effects of Multiphase Flow on Internal CO2 Corrosion of Mild Steel Pipelines. Energy & Fuels, 2012. **26**(7): p. 4098-4111.
11. Sun, W., K. Chokshi, and S. Nesic, Iron Carbonate Scale Growth and the Effect of Inhibition in CO_2 Corrosion of Mild Steel, CORROSION 2005. 2005. NACE International.
12. Pessu, F., R. Barker, and A. Neville. The influence of pH on localized corrosion behavior of X65 carbon steel in CO_2-saturated brines. CORROSION 2015. 2015. NACE International.
13. Tanupabrungsun, T., B. Brown, and S. Nesic, Effect of pH on CO_2 corrosion of mild steel at elevated temperatures. CORROSION 2013, 2013(48).
14. Li, W., B. Brown, D. Young, and S. Nešic, Investigation of pseudo-passivation of mild steel in CO_2 corrosion. Corrosion, 2013. **70**(3): p. 294-302.
15. Burkle, D., R. De Motte, W. Taleb, A. Kleppe, T. Comyn, S. Vargas, A. Neville, and R. Barker, Development of an electrochemically integrated SR-GIXRD flow cell to study FeCO3 formation kinetics. Review of Scientific Instruments, 2016. **87**(10): p. 105125.
16. De Marco, R., Z.-T. Jiang, D. John, M. Sercombe, and B. Kinsella, An in situ electrochemical impedance spectroscopy/synchrotron radiation grazing incidence X-ray diffraction study of the influence of acetate on the carbon dioxide corrosion of mild steel. Electrochimica acta, 2007. **52**(11): p. 3746-3750.
17. De Marco, R., Z.-T. Jiang, B. Pejcic, and E. Poinen, An in situ synchrotron radiation grazing incidence X-ray diffraction study of carbon dioxide corrosion. Journal of The Electrochemical Society, 2005. **152**(10): p. B389-B392.

18. Ingham, B., M. Ko, G. Kear, P. Kappen, N. Laycock, J. Kimpton, and D. Williams, In situ synchrotron X-ray diffraction study of surface scale formation during CO 2 corrosion of carbon steel at temperatures up to 90 C. Corrosion Science, 2010. **52**(9): p. 3052-3061.

19. Ingham, B., M. Ko, N. Laycock, N.M. Kirby, and D.E. Williams, First stages of siderite crystallisation during CO 2 corrosion of steel evaluated using in situ synchrotron small-and wide-angle X-ray scattering. Faraday discussions, 2015. **180**: p. 171-190.

20. Joshi, G.R., K. Cooper, J. Lapinski, D.L. Engelberg, O. Bikondoa, M.G. Dowsett, and R. Lindsay. In Situ Grazing Incidence X-ray Diffraction of Sweet Corrosion Scaling on Carbon Steel. in CORROSION 2015. 2015. NACE International.

21. Han, J., D. Young, H. Colijn, A. Tripathi, and S. Nešić, Chemistry and structure of the passive film on mild steel in CO2 corrosion environments. Industrial & Engineering Chemistry Research, 2009. **48**(13): p. 6296-6302.

22. Sanni, O., T. Charpentier, N. Kapur, and A. Neville. Study of surface deposition and bulk scaling kinetics in oilfield conditions using an in-situ flow rig. NACE-International Corrosion Conference Series. 2015.

23. Oddo, J.E. and M.B. Tomson, Simplified calculation of CaCO3 saturation at high temperatures and pressures in brine solutions. Journal of Petroleum Technology, 1982. **34**(07): p. 1,583-1,590.

24. Kharaka, Y.K., W.D. Gunter, P.K. Aggarwal, E.H. Perkins, and J.D. DeBraal, SOLMINEQ. 88: A computer program for geochemical modeling of water-rock interactions. US geological survey water-resources investigation report, 1988. **88**: p. 4227.

25. Palmer, D.A. and R. Van Eldik, The chemistry of metal carbonato and carbon dioxide complexes. Chemical Reviews, 1983. **83**(6): p. 651-731.

26. Sun, W., S. Nesic, and R.C. Woollam, The effect of temperature and ionic strength on iron carbonate ($FeCO_3$) solubility limit. Corrosion Science, 2009. **51**(6): p. 1273-1276.

27. Dugstad, A., The importance of $FeCO_3$ supersaturation on the CO_2 corrosion of mild steels. Corrosion 1992. **92**(14).

28. Sun, W. and S. Nesic, Kinetics of corrosion layer formation: part 1—iron carbonate layers in carbon dioxide corrosion. Corrosion, 2008. **64**(4): p. 334-346.

29. Nešic, S. and K.-L. Lee, A mechanistic model for carbon dioxide corrosion of mild steel in the presence of protective iron carbonate films—part 3: film growth model. Corrosion, 2003. **59**(7): p. 616-628.

30. Gao, M., X. Pang, and K. Gao, The growth mechanism of CO 2 corrosion product films. Corrosion Science, 2011. **53**(2): p. 557-568.

31. Linter, B. and G. Burstein, Reactions of pipeline steels in carbon dioxide solutions. Corrosion science, 1999. **41**(1): p. 117-139.

32. Johnson, M. and M. Tomson, Ferrous Carbonate Precipitation Kinetics and its Impact on CO2 Corrosion. Corrosion, 1991(268).

33. Greenberg, J. and M. Tomson, Precipitation and dissolution kinetics and equilibria of aqueous ferrous carbonate vs temperature. Applied Geochemistry, 1992. **7**(2): p. 185-190.